# Two Families of Rare-Earth-Substituted Dawson-type Monomeric and Dimeric Phosphotungstates Functionalized by Carboxylic Ligands

Xiuhua Wang,[†] Yajie Liu,[†] Mengtian Jin,[†] Yuxing Wu,[†] Lijuan Chen,*,[†] and Jun-Wei Zhao*,[†,‡]

[†]Henan Key Laboratory of Polyoxometalate Chemistry, Institute of Molecular and Crystal Engineering, College of Chemistry and Chemical Engineering, Henan University, Kaifeng, Henan 475004, People's Republic of China

[‡]State Key Laboratory of Structural Chemistry, Fujian Institute of Research on the Structure of Matter, Chinese Academy of Sciences, Fuzhou, Fujian 350002, People's Republic of China

Ⓢ Supporting Information

**ABSTRACT:** Two series of novel organic—inorganic hybrid carboxylated rare-earth-substituted monolacunary Dawson-type phosphotungstate monomers $[Hdap]_4[RE(H_2O)(Hpic)_3][RE(Hpic)_2(\alpha_2-P_2W_{17}O_{61})]\cdot 21H_2O$ [RE = $Gd^{III}$ (**1**), $Tb^{III}$ (**2**), $Dy^{III}$ (**3**), $Ho^{III}$ (**4**), $Er^{III}$ (**5**), $Tm^{III}$ (**6**), $Yb^{III}$ (**7**), $Y^{III}$ (**8**); Hpic = 2-picolinic acid, dap = 1,2-diaminopropane] and dimers $[H_2dap]_8[RE_2(H_2ox)_2(ox)(\alpha_2-P_2W_{17}O_{61})_2]\cdot 25H_2O$ [RE = $Ho^{III}$ (**9**), $Er^{III}$ (**10**), $Tm^{III}$ (**11**), $Yb^{III}$ (**12**), $Y^{III}$ (**13**); $H_2ox$ = oxalic acid] have been hydrothermally synthesized and characterized by elemental analyses, IR spectra, thermogravimetric measurements, and X-ray single-crystal diffraction. The monomeric polyoxoanion skeleton of isomorphic **1−8** is constructed from a monolacunary Dawson-type phosphotungstate implanted by a $[RE1(Hpic)_2]^{3+}$ cation in the polar position and supported by the other $[RE2(H_2O)(Hpic)_3]^{3+}$ cation on the equatorial belt. Interestingly, two kinds of RE cations separately coordinate to two or three Hpic ligands in the form of N−C−C−O−RE containing five-membered ring fashion. The dimeric polyoxoanion backbone of isomorphic **9−13** is built by two mono-RE substituted Dawson-type phosphotungstate fragments $[RE(H_2ox)(\alpha_2-P_2W_{17}O_{61})]^{7-}$ joined together by an $ox^{2-}$ linker. The visible photoluminescence spectra of solid-state **2**, **3**, **5**, and **10** and the NIR photoluminescence properties for solid-state **5**, **10**, **7**, and **12** at ambient temperature have been carried out, which are mainly derived from the $RE^{3+}$ f−f electron transitions. Magnetic susceptibility measurements and fitting results of **3** demonstrate that **3** is a single-molecule magnet.
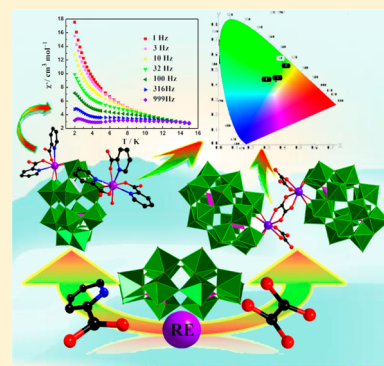
## INTRODUCTION

Polyoxometalate (POM)-based functional materials have attracted a high level of interest because of unique structural and compositional varieties and potential applications in catalysis, magnetism, medicine, biology, material science, electrochromism, and photoluminescence.[1−11] With the nucleophilic oxygen-enriched surfaces and high negative charges, POM building blocks (especially for lacunary Keggin-/Dawson-type polyoxotungstates (POTs)) can serve as the prominent multidentate inorganic chelating ligands and bind most of transition-metal (TM) or rare-earth (RE) cations to design and synthesize novel polynuclear TM or RE substituted POM-based functional materials.[12−14] As oxyphile RE cations always can transfer their functionalities such as magnetic, luminescent, or Lewis acid catalytic properties to the desired materials,[15−18] more and more chemists are prone to incorporate RE cations into diverse POM matrixes to prepare an array of novel RE substituted POM-based functional materials combining the unique properties of both components.[19−55] Since Peacock and Weakley initiated the investigations on lacunary Keggin- and Dawson-type RE-substituted POM-based materials (RESPMs) in 1971,[19] a large number of Peacock−Weakley-type mononuclear

RESPMs (1:2-type) $[RE(XW_{11}O_{39})_2]^{n-}$ (X = $P^V$, $Si^{IV}$, $Ge^{IV}$, $As^V$) with discrete structures have been reported.[20−23] In 2001, Pope et al. first communicated the one-dimensional (1-D) chain RESPMs $[RE(\alpha-SiW_{11}O_{39})(H_2O)_3]^{5-}$ (RE = $Ce^{III}$, $La^{III}$),[24] and then other analogues with extended structures were successively discovered.[25−27] In 2007, Kortz et al. addressed the first series of chiral RESPMs $[RE(\beta_2-SiW_{11}O_{39})_2]^{13-}$ (RE = $La^{III}$, $Ce^{III}$, $Sm^{III}$, $Eu^{III}$, $Gd^{III}$, $Tb^{III}$, $Yb^{III}$, $Lu^{III}$)[28] and a giant 20-$Ce^{III}$-containing tungstogermanate $[Ce_{20}Ge_{10}W_{100}O_{376}(OH)_4(H_2O)_{30}]^{56-}$.[29] In 2009, Boskovic and co-workers obtained a high-nuclear $Gd^{III}$ encapsulated polytungstoarsenate $[Gd_6As_6W_{65}O_{229}(OH)_4(H_2O)_{12}(OAc)_2]^{38-}$,[30] and Niu's group reported 2:2-type monovacant Keggin phosphotungstate dimers $[\{(\alpha-PW_{11}O_{39}H)RE(H_2O)_3\}_2]^{6-}$ (RE = $Nd^{III}$, $Gd^{III}$).[31] Subsequently, reports on RESPMs have undergone an explosive growth, such as the giant crown-shaped-ring $[K\subset K_7Ce_{24}Ge_{12}W_{120}O_{456}(OH)_{12}(H_2O)_{64}]^{52-}$,[32] 1-D chain $[Nd_3As_4W_{41}O_{141}OH(H_2O)_{10}]^{16-}$,[33] hexadeca-RE-encapsulated $[RE_{16}As_{16}W_{164}O_{576}(OH)_8(H_2O)_{42}]^{80-}$

(RE = Eu$^{III}$, Gd$^{III}$, Tb$^{III}$, Dy$^{III}$, Ho$^{III}$),[34] and Bi$_6$-containing [[(BiW$_9$O$_{33}$)$_4$(WO$_3$){Bi$_6$($\mu_3$-O)$_4$($\mu_2$-OH)$_3$} (RE$_3$(H$_2$O)$_6$CO$_3$)]$^{22-}$ (RE = Pr$^{III}$, Nd$^{III}$, La$^{III}$).[35] Moreover, outstanding progress on organic−inorganic hybrid RESPMs has been also made. For instance, in 2011, Kortz and collaborators synthesized an acetate-containing tri-Y$^{III}$-incorporated tungstoantimonate [{Y($\alpha$-SbW$_9$O$_{31}$(OH)$_2$)(CH$_3$COO)(H$_2$O)}$_3$(WO$_4$)]$^{17-}$,[36] and Boskovic's group synthesized and characterized the first POT-supported polynuclear Ln-based single-molecule magnet (SMM) [Dy$_4$As$_5$W$_{40}$O$_{144}$(H$_2$O)$_{10}$(gly)$_2$]$^{21-}$ (gly = glycine).[37] In 2012, Niu's group separated a family of oxalate-connective RE-substituted Keggin-type phosphotungstates {[($\alpha$-PW$_{11}$O$_{39}$)RE-(H$_2$O)$_2$(C$_2$O$_4$)}$^{10-}$ (RE = Y$^{III}$, Dy$^{III}$, Ho$^{III}$, Er$^{III}$) and {($\alpha$-x-PW$_{10}$O$_{38}$)Tm$_2$(C$_2$O$_4$)(H$_2$O)$_2$}$^{3-}$,[38] and obtained a three-dimensional (3-D) extended framework [RE(HL)(L)(H$_2$O)$_6${RE-(H$_2$L)$_{0.5}$($\alpha$-PW$_{11}$O$_{39}$H)RE(H$_2$O)$_4$]}$_2$ (RE = La$^{III}$, Ce$^{III}$, H$_2$L = 2,5-pyridinedicarboxylic acid) displaying the photocatalytic degradation activity for rhodamine-B.[39] In 2014, Boskovic et al. discovered the first modular family of amino-acid−POM hybrids [As$^{III}$$_4$(Y$^{III}$W$^{VI}$$_3$)W$^{VI}$$_{44}$Y$^{III}$$_4$O$_{159}$(gly)$_8$(H$_2$O)$_{14}$]$^{9-}$ and [As$^{III}$$_4$-(Mo$^V$$_2$Mo$^{VI}$$_2$)W$^{VI}$$_{44}$Y$^{III}$$_4$O$_{160}$(nle)$_9$(H$_2$O)$_{11}$][As$^{III}$$_4$(Mo$^{VI}$$_2$W$^{VI}$$_2$)-W$^{VI}$$_{44}$Y$^{III}$$_4$O$_{160}$(nle)$_9$(H$_2$O)$_{11}$]$^{18-}$, which exhibit the site-selective metal substitution and photoreduction of the tetranuclear core of the hybrid polyoxoanions.[40] In 2015, Niu et al. synthesized a series of citric-acid-containing RESPMs [RE$_3$(H$_2$O)$_7$-{RE$_2$(H$_2$O)$_4$As$_2$W$_{19}$O$_{68}$(WO$_2$)$_2$(C$_6$O$_7$H$_4$)$_2$}$_3$]$^{33-}$ (RE = Y$^{III}$, Tb$^{III}$, Dy$^{III}$, Ho$^{III}$, Er$^{III}$, Tm$^{III}$, Yb$^{III}$, Lu$^{III}$).[41] Recently, our group obtained a class of trigonal pyramidal {AsO$_2$(OH)}-bridging RE substituted arsenotungstates {[W$_3$RE$_2$(H$_2$O)$_8$-AsO$_8$(OH)][B-$\alpha$-AsW$_9$O$_{33}$]$_2$}$^{16-}$ (RE = Eu$^{III}$, Gd$^{III}$, Tb$^{III}$, Dy$^{III}$, Ho$^{III}$, Y$^{III}$),[42] and three types of Ser-decorated RE-containing arsenotungstates [RE$_2$W$_4$O$_{10}$(H$_2$O)$_8$(Ser)$_2$(B-$\alpha$-AsW$_9$-O$_{33}$)$_2$]$^{8-}$ (RE = Eu$^{III}$, Gd$^{III}$, Tb$^{III}$, Dy$^{III}$, Ho$^{III}$, Er$^{III}$, Tm$^{III}$, Y$^{III}$), [RE$_4$W$_8$O$_{19}$(H$_2$O)$_{10}$(OH)$_2$(Ser)$_2$(B-$\alpha$-AsW$_9$O$_{33}$)$_4$]$^{16-}$ (RE = Dy$^{III}$, Ho$^{III}$, Er$^{III}$, Yb$^{III}$, Y$^{III}$) and [RE$_4$W$_8$O$_{19}$(H$_2$O)$_8$(OH)$_2$-(Ser)$_4$(B-$\alpha$-AsW$_9$O$_{33}$)$_4$]$^{16-}$ (RE = Ce$^{III}$, Pr$^{III}$) (Ser = serine) and investigated their solid-state luminescence properties.[43]

In contrast to Keggin-type RESPMs, systematic explorations and relevant reports on Dawson-type RESPMs are relatively rare. For instance, in 2001, Pope et al. obtained a centrosymmetric head-to-head dimer [{Ce(H$_2$O)$_4$(P$_2$W$_{17}$O$_{61}$)}$_2$]$^{14-}$.[44] In 2005 Hill and co-workers isolated a sandwich-type POT-supported hydroxo/oxo cluster [{Yb$_6$($\mu_6$-O)($\mu_3$-OH)$_6$(H$_2$O)$_6$}($\alpha$-P$_2$W$_{15}$O$_{56}$)$_2$]$^{14-}$ anchoring a trigonal antiprismatic hexa-Yb$^{III}$ core.[45] In 2006, Wang's group made the first 1-D and two-dimensional (2-D) Dawson-type RESPMs [Nd$_3$(H$_2$O)$_{17}$($\alpha_2$-P$_2$W$_{17}$O$_{61}$)]$^-$ and [Nd$_2$(H$_2$O)$_9$ ($\alpha_2$-P$_2$W$_{17}$O$_{61}$)]$^{4-}$.[46] In 2007, Pope and collaborators addressed the 3-D frameworks based on [K⊂P$_8$W$_{48}$O$_{184}$(H$_4$W$_4$O$_{12}$)$_2$RE$_2$(H$_2$O)$_{10}$]$^{25-}$ (RE = La$^{III}$, Ce$^{III}$, Pr$^{III}$, Nd$^{III}$) in the presence of the [P$_8$W$_{48}$O$_{184}$]$^{40-}$ precursor and RE cations.[47] Later, Yang et al. isolated two {P$_8$W$_{48}$O$_{184}$}-containing RESPMs {[RE$_2$($\mu$-OH)$_4$(H$_2$O)$_{12}$]$_2$(H$_{24}$P$_8$W$_{48}$O$_{184}$)}$^{12-}$ (RE = Sm$^{III}$, Tb$^{III}$).[48] In 2011, Patzke et al. isolated the first open Dawson RE encapsulated silicotungstates [RE$_2$(H$_2$O)$_7$-Si$_2$W$_{18}$O$_{66}$]$^{10-}$ (RE = Tb$^{III}$, Ho$^{III}$) in the sodium acetate buffer.[49] In 2013 and 2016, Niu's group obtained a monovacant Dawson-type hexameric RESPM {Na$_{12}$[($\alpha_2$-P$_2$W$_{17}$O$_{61}$H$_2$)La(H$_2$O)$_4$]$_6$}$^{6-}$,[50] and a mixed-valence Ce$_{10}$-embedded Dawson trimer {[Ce$^{IV}$$_7$Ce$^{III}$$_3$O$_6$(OH)$_6$(CO$_3$)(H$_2$O)$_{11}$][(P$_2$W$_{16}$O$_{59}$)]$_3$}$^{19-}$.[51] Besides, a few organic−inorganic Dawson-type RESPMs with carboxylic ligands were also reported. For example, in 2003, Kortz reported a head-on dimer [{La(CH$_3$COO)(H$_2$O)$_2$($\alpha_2$-P$_2$W$_{17}$O$_{61}$)}$_2$]$^{16-}$ consisting of two [$\alpha_2$-P$_2$W$_{17}$O$_{61}$]$^{10-}$ moieties bridged by a

[La$_2$(CH$_3$COO)$_2$(H$_2$O)$_4$]$^{4+}$ ion.[52] In 2006, Mialane et al. isolated a tetrameric species [{Yb(P$_2$W$_{17}$O$_{61}$)}$_4$(C$_2$O$_4$)$_3$(H$_2$O)$_4$]$^{34-}$ built from four [Yb(H$_2$O)$_4$(P$_2$W$_{17}$O$_{61}$)]$^{7-}$ units linked by four oxalate ligands.[53] In 2014, Xu and co-workers isolated two enantiomers {Na⊂[Ce$^{III}$(H$_2$O)(CH$_3$CH$_2$OH)(L-tartH$_3$)(H$_2$Si$_2$W$_{19}$O$_{66}$)]}$^{5-}$ and {Na⊂[Ce$^{III}$(H$_2$O)(CH$_3$CH$_2$OH)(D-tartH$_3$)(Si$_2$W$_{19}$O$_{66}$)]}$^{7-}$ (tartH$_4$ = tartaric acid).[54] In 2016, Niu et al. addressed an uncommon zigzag tetrameric RESPM [{Ce($\eta^1$-C$_6$H$_5$NO$_2$)$_2$(H$_2$O)$_6$[Ce-(H$_2$O)$_3$($\alpha_2$-P$_2$W$_{17}$O$_{61}$)]}{Ce($\eta_2$-C$_6$H$_5$NO$_2$)$_2$(H$_2$O)$_5$[Ce(H$_2$O)-($\alpha_2$-P$_2$W$_{17}$O$_{61}$)]}]$_2$$^{24-}$ (C$_6$H$_5$NO$_2$ = isonicotinic acid).[55]

All in all, the reported Dawson-type RESPMs are less than those Keggin-type species. It is extremely obvious that investigations on organic−inorganic hybrid Dawson-type RESPMs with carboxylic components are much less developed. Therefore, the continuous search and elaborate preparation of carboxylate-encapsulated Dawson-type RESPMs remain a great challenge. In general, Ln-POM complexes are usually considered as discrete molecular complexes of RE phosphors, which can be sensitized by intramolecular energy transfer from the O → M (M = Mo or W) excited states to excited energy levels of the RE ions.[56] On one hand, organic carboxylic ligands can be endowed with some functionalities especially in luminescence sensitization and magnetic exchange interaction when they are introduced to RESPMs.[57] On the other hand, the flexible bonding modes of CO$_2^-$ groups such as monodentate, chelating mode, etc. will be apt to construct diverse structures of RESPMs. In addition, the hexavacant [H$_2$P$_2$W$_{12}$O$_{48}$]$^{12-}$-{P$_2$W$_{12}$} precursor derived from the degradation of the plenary Dawson [$\alpha$-P$_2$W$_{18}$O$_{62}$]$^{6-}$ cluster can transform to dimeric {P$_4$W$_{24}$},[58] trimeric {P$_6$W$_{36}$},[59−62] tetrameric {P$_8$W$_{48}$},[63,64] tetravacant {P$_2$W$_{14}$},[65,66] or monovacant {P$_2$W$_{17}$}.[67,68] Hence, the {P$_2$W$_{12}$} precursor catches our attention and is used by us to prepare novel carboxylate-encapsulated RESPMs. However, the common phenomenon always happen that the reaction of the hexavacant {P$_2$W$_{12}$} precursor with RE ions in aqueous solution often leads to precipitate phases.[69] As a result, the hydrothermal technique has been employed to solve the problem. To obtain novel organic−inorganic hybrid Dawson-type RESPMs with carboxylate ligands, we choose {P$_2$W$_{12}$} as the precursor and 2-picolinic acid (Hpic) as the organic ligand to react with rare-earth nitrate under hydrothermal conditions and successfully isolated a series of RE-substituted monovacant Dawson-type monomeric phosphotungstates modified by Hpic ligands [Hdap]$_4$[RE(H$_2$O)(Hpic)$_3$][RE(Hpic)$_2$($\alpha_2$-P$_2$W$_{17}$-O$_{61}$)]·21H$_2$O [RE = Gd$^{III}$ (1), Tb$^{III}$ (2), Dy$^{III}$ (3), Ho$^{III}$ (4), Er$^{III}$ (5), Tm$^{III}$ (6), Yb$^{III}$ (7), Y$^{III}$ (8)]. Interestingly, when Hpic was replaced by oxalate acid (H$_2$ox), a family of RE-substituted monovacant Dawson-type dimeric phosphotungstates decorated by oxalate ligands [H$_2$dap]$_7$H$_2$[RE$_2$(H$_2$ox)$_2$(ox)($\alpha_2$-P$_2$W$_{17}$O$_{61}$)$_2$]·22H$_2$O [RE = Ho$^{III}$ (9), Er$^{III}$ (10), Tm$^{III}$ (11), Yb$^{III}$ (12), Y$^{III}$ (13)] were isolated. The monomeric polyoxoanion skeleton {[RE(H$_2$O)(Hpic)$_3$][RE(Hpic)$_2$($\alpha_2$-P$_2$W$_{17}$O$_{61}$)]}$^{4-}$ of 1−8 consists of a monovacant Dawson-type [$\alpha_2$-P$_2$W$_{17}$O$_{61}$]$^{10-}$ fragment, a di-Hpic-chelating [RE(Hpic)$_2$]$^{3+}$ cation and a tri-Hpic-chelating [RE(H$_2$O)(Hpic)$_3$]$^{3+}$ cation whereas the dimeric S-shaped polyoxoanion backbone [RE$_2$(H$_2$ox)$_2$(ox)($\alpha_2$-P$_2$W$_{17}$O$_{61}$)$_2$]$^{16-}$ of 9−13 comprises two mono-RE substituted Dawson-type [RE(H$_2$ox)($\alpha_2$-PW$_{17}$O$_{61}$)]$^{7-}$ units bridged by an oxalate connector. The visible photoluminescence spectra and lifetime decay behaviors of solid-state 2, 3, 5, and 10 and the NIR photoluminescence properties for solid-state 5, 10, 7, and 12 at ambient temperature have been carried out, which exhibit the RE$^{3+}$ f−f electron transitions. Moreover, we have also compared

the luminescence properties of different Er$^{III}$- or Yb$^{III}$-analogues decorated with 2-picolinic acid or oxalic acid upon photo-excitation in the visible or NIR region at room temperature and the emission intensity of Hpic-RESPMs are stronger than ox-RESPMs. The magnetic susceptibility properties of **3** have been studied in the temperature range of 2−300 K. The alternate-current (*ac*) magnetic susceptibility measurements and the fitting results of the Debye model and the Arrhenius law manifest that **3** displays SMM behavior.

## ■ EXPERIMENTAL SECTION

**Materials and Methods.** K$_{12}$[H$_2$P$_2$W$_{12}$O$_{48}$]·24H$_2$O was synthesized according to the published procedure.[70] All other reagents were used as purchased without further purification. IR spectra were recorded from solid samples palletized with KBr on a Nicolet 170 SXFT−IR spectrometer in the range of 4000−400 cm$^{-1}$. Thermogravimetric (TG) analyses were performed on a Mettler−Toledo TGA/SDTA 851$^e$ thermal analyzer in flowing N$_2$ at a heating rate of 10 °C min$^{-1}$ from 25 to 900 °C. Carbon, hydrogen, and nitrogen elemental analyses were carried out on a PerkinElmer 2400-II CHNS/O analyzer. Inductively coupled plasma atomic emission spectrometry measurements were made on a PerkinElmer Optima 2000 ICP-AES spectrometer. Powder X-ray diffraction (PXRD) spectra were performed based on a Bruker D8 ADVANCE instrument with Cu Kα radiation (λ = 1.54056 Å) in the angular range of 2θ = 5−50 ° at room temperature. Photoluminescence spectra and lifetimes were recorded using an FLS 980 Edinburgh Analytical Instrument apparatus equipped with a 450 W xenon lamp and a μF900H high-energy microsecond flash lamp as the excitation sources. Magnetic measurements were taken out on a Quantum Design SQUID (MPMS XL 7) magnetometer.

**Syntheses of [Hdap]$_4$[RE(H$_2$O)(Hpic)$_3$][RE(Hpic)$_2$(α$_2$-P$_2$W$_{17}$O$_{61}$)]·21H$_2$O [RE = Gd$^{III}$ (1), Tb$^{III}$ (2), Dy$^{III}$ (3), Ho$^{III}$ (4), Er$^{III}$ (5), Tm$^{III}$ (6), Yb$^{III}$ (7), Y$^{III}$ (8)].** K$_{12}$[H$_2$P$_2$W$_{12}$O$_{48}$]·24H$_2$O (0.284 g, 0.072 mmol), Hpic (0.105 g, 0.853 mmol), and Gd(NO$_3$)$_3$·6H$_2$O (0.114 g, 0.253 mmol), Tb(NO$_3$)$_3$·6H$_2$O (0.108 g, 0.238 mmol), Dy(NO$_3$)$_3$·6H$_2$O (0.110 g, 0.241 mmol), Ho(NO$_3$)$_3$·6H$_2$O (0.109 g, 0.238 mmol), Er(NO$_3$)$_3$·6H$_2$O (0.133 g, 0.288 mmol), Tm(NO$_3$)$_3$·6H$_2$O (0.112 g, 0.242 mmol), Yb(NO$_3$)$_3$·6H$_2$O (0.121 g, 0.259 mmol), or Y(NO$_3$)$_3$·6H$_2$O (0.108 g, 0.282 mmol) were suspended in distilled water (10 mL) and stirred for 5 min, and then dap (0.150 mL, 1.761 mmol) was added under stirring. After 10 min, a NaCl aqueous solution (1.0 mL, 1.0 mol L$^{-1}$) was dropwise added. Upon continuous stirring for 20 min, the pH value of the mixture was adjusted to 5−6 by 2 mol L$^{-1}$ NaOH solution. The resulting mixture was transferred to a 25 mL Teflon-lined steel autoclave, heated under autogenous pressure at 80 °C for a week, and then naturally cooled to room temperature in air. Colorless rod-like crystals for **1**, pale yellow rod-like crystals for **2**, colorless rod-like crystals for **3**, light yellow rod-like crystals for **4**, pink rod-like crystals for **5**, pale green rod-like crystals for **6**, colorless rod-like crystals for **7** and colorless rod-like crystals for **8** were obtained by filtration, washed with distilled water, and dried in air. Yield: ca. 26%, 25%, 25%, 26%, 28%, 24%, 28%, and 22% based on K$_{12}$[H$_2$P$_2$W$_{12}$O$_{48}$]·24H$_2$O for **1**, **2**, **3**, **4**, **5**, **6**, **7**, and **8** respectively. Anal. Calcd (found %) for C$_{42}$H$_{113}$N$_{13}$O$_{93}$ Gd$_2$P$_2$W$_{17}$ (**1**): C 8.71 (9.11), H 1.97 (1.911), N 3.14 (3.36), Gd 5.43 (5.20), W 53.98 (54.14); for C$_{42}$H$_{113}$N$_{13}$O$_{93}$Tb$_2$P$_2$W$_{17}$ (**2**): C 8.71 (9.16), H 1.97 (1.912), N 3.14 (3.29), Tb 5.49 (5.27), W 53.95 (54.04); for C$_{42}$H$_{113}$N$_{13}$O$_{93}$Dy$_2$P$_2$W$_{17}$ (**3**): C 8.70 (9.06), H 1.96 (1.909), N 3.14 (3.41), Dy 5.60 (5.25), W 53.88 (54.10); for C$_{42}$H$_{113}$N$_{13}$O$_{93}$Ho$_2$P$_2$W$_{17}$ (**4**): C 8.69 (9.06), H 1.96 (1.908), N 3.14 (3.27), Ho 5.68 (5.31), W 53.83 (54.05); for C$_{42}$H$_{113}$N$_{13}$O$_{93}$Er$_2$P$_2$W$_{17}$ (**5**): C 8.68 (9.01), H 1.96 (1.90), N 3.13 (3.28), Er 5.76 (5.46), W 53.79 (54.01); for C$_{42}$H$_{113}$N$_{13}$O$_{93}$Tm$_2$P$_2$W$_{17}$ (**6**): C 8.68 (9.08), H 1.96 (1.95), N 3.13 (3.31), Tm 5.81 (5.52), W 53.76 (54.08); for C$_{42}$H$_{113}$N$_{13}$O$_{93}$Yb$_2$P$_2$W$_{17}$ (**7**): C 8.67 (9.11), H 1.96 (1.92), N 3.13 (3.16), Yb 5.94 (5.57), W 53.68 (53.99); for C$_{42}$H$_{113}$N$_{13}$O$_{93}$Y$_2$P$_2$W$_{17}$ (**8**): C 8.92 (9.06), H 2.01 (1.99), N 3.22 (3.39), Y 5.94 (5.85), W 55.28 (55.47). IR bands (cm$^{-1}$) for **1**: 3437s, 3092m, 2933m, 1623m, 1591s, 1564m, 1512w, 1474w, 1444w,

1387m, 1297w, 1244w, 1162w, 1084s, 1058w, 1017w, 940s, 919w, 861w, 800s, 704m, 637w, 524m; for **2**: 3439s, 3092m, 2939m, 1620m, 1591s, 1564m, 1514w, 1476w, 1445w, 1387m, 1297w, 1243w, 1161w, 1084s, 1058w, 1017w, 940s, 919w, 861w, 800s, 704m, 638w, 528m; for **3**: 3443s, 3097m, 2935m, 1623m, 1593s, 1566m, 1514w, 1477w, 1445w, 1387m, 1297w, 1244w, 1169w, 1084s, 1058w, 1017w, 940s, 919w, 861w, 800s, 704m, 636w, 523m; for **4**: 3443s, 3093m, 2939m, 1619m, 1591s, 1568m, 1514w, 1471w, 1445w, 1387m, 1293w, 1243w, 1163w, 1083s, 1053w, 1015w, 940s, 915w, 861w, 804s, 706m, 636w, 521m; for **5**: 3443s, 3096m, 2940m, 1626m, 1591s, 1564m, 1513w, 1477w, 1445w, 1387m, 1297w, 1242w, 1165w, 1083s, 1054w, 1015w, 940s, 915w, 866w, 800s, 706m, 637w, 525m; for **6**: 3443s, 3089m, 2937m, 1625m, 1594s, 1568m, 1514w, 1476w, 1445w, 1389m, 1299w, 1244w, 1169w, 1086s, 1054w, 1015w, 941s, 919w, 864w, 806s, 706m, 631w, 523m; for **7**: 3443s, 3094m, 2935m, 1625m, 1593s, 1566m, 1514w, 1477w, 1445w, 1387m, 1297w, 1244w, 1169w, 1084s, 1058w, 1017w, 940s, 919w, 861w, 800s, 704m, 639w, 524m; for **8**: 3443s, 3096m, 2939m, 1621m, 1589s, 1562m, 1513w, 1477w, 1445w, 1389m, 1297w, 1244w, 1169w, 1084s, 1058w, 1017w, 940s, 919w, 861w, 806s, 706m, 633w, 523m, respectively (Figure S1a, Supporting Information).

**Syntheses of [H$_2$dap]$_8$[Ho$_2$(H$_2$ox)$_2$(ox)(α$_2$-P$_2$W$_{17}$O$_{61}$)$_2$]·25 H$_2$O [RE = Ho$^{III}$ (9), Er$^{III}$ (10), Tm$^{III}$ (11), Yb$^{III}$ (12), Y$^{III}$ (13)].** A mixture of K$_{12}$[H$_2$P$_2$W$_{12}$O$_{48}$]·24H$_2$O (0.280 g, 0.071 mmol), H$_2$C$_2$O$_4$·2H$_2$O (0.213 g, 1.689 mmol), and Ho(NO$_3$)$_3$·6H$_2$O (0.122 g, 0.266 mmol), Er(NO$_3$)$_3$·6H$_2$O (0.116 g, 0.242 mmol), Tm(NO$_3$)$_3$·6H$_2$O (0.111 g, 0.239 mmol), Yb(NO$_3$)$_3$·6H$_2$O (0.120 g, 0.248 mmol), or Y(NO$_3$)$_3$·6 H$_2$O (0.101 g, 0.264 mmol) for **9**, **10**, **11**, **12**, or **13** was stirred in distilled water (10 mL) for 5 min, and then dap (0.150 mL, 1.761 mmol) was added under stirring. After 10 min, an aqueous solution (1 mL) of 1 mol L$^{-1}$ NaCl was dropwise added. Upon continuous stirring for 20 min, the pH value of the mixture was adjusted to 5−6 with 2 mol L$^{-1}$ NaOH solution. The resulting mixture was transferred into a 25 mL Teflon-lined steel autoclave, heated under autogenous pressure at 80 °C for a week, and then cooled to room temperature naturally in air. Light yellow block crystals were obtained by filtration, washed with distilled water and dried in air. Yield: ca. 25%, 30%, 15%, 26%, and 30% based on K$_{12}$[H$_2$P$_2$W$_{12}$O$_{48}$]·24H$_2$O for **9**, **10**, **11**, **12** and **13**, respectively. Anal. Calcd (found %) for **9**, C$_{30}$H$_{150}$N$_{16}$O$_{159}$Ho$_2$P$_4$W$_{34}$: C 3.61 (3.91), H 1.53 (1.72), N 2.24 (2.42), Ho 3.30 (3.07), W 62.61 (62.40); for **10**, C$_{30}$H$_{150}$N$_{16}$O$_{159}$Er$_2$P$_4$W$_{34}$: C 3.61 (3.89), H 1.53(1.67), N 2.24 (2.44), Er 3.35 (3.14), W 62.58 (62.44); for **11**, C$_{30}$H$_{150}$N$_{16}$O$_{159}$Tm$_2$P$_4$W$_{34}$: C 3.60 (3.87), H 1.53 (1.67), N 2.24 (2.43), Tm 3.38 (3.02), W 62.56 (62.35); for **12**, C$_{30}$H$_{150}$N$_{16}$O$_{159}$ Yb$_2$P$_4$W$_{34}$: C 3.60 (3.83), H 1.53 (1.70), N 2.24 (2.46), Yb 3.46 (3.09), W 62.51 (62.60); for **13**, C$_{30}$H$_{150}$N$_{16}$O$_{159}$Y$_2$P$_4$W$_{34}$: C 3.66 (3.91), H 1.56 (1.72), N 2.28 (2.43), Y 1.81 (2.07), W 63.58 (63.39). IR bands (cm$^{-1}$) for **9**: 3407s, 3171m, 2957m, 1677m, 1625s, 1510m, 1457m, 1410w, 1363w, 1322m, 1084s, 1054w, 1022w, 938s, 923w, 870w,782s, 724m, 524s; for **10**: 3446s, 3171m, 2938m, 1677m, 1619s, 1510m, 1451m, 1410w, 1363w, 1322m, 1084s, 1054w, 1022w, 943s, 911w, 876w,782s, 708m, 524s; for **11**: 3416s, 3171m, 2968m, 1683m, 1625s, 1510m, 1457m, 1410w, 1363w, 1322m, 1084s,1054w, 1022w, 943s, 923w, 876w,782s, 714m, 526s; for **12**: 3458s, 3181m, 2978m, 1677m, 1630s, 1510m, 1451m, 1416w, 1369w, 1325m, 1084s, 1054w, 1022w, 943s, 911w, 864w,787s, 714m, 524s; for **13**: 3467s, 3162m, 2998m, 1683m, 1623s, 1510m, 1457m, 1410w, 1369w, 1322m, 1084s, 1054w, 1022w, 938s, 917w, 879w, 782s, 714m, 524s, respectively (Figure S1b, Supporting Information).

**X-ray Crystallography.** A suitable single crystal for **1−13** was selected and placed on a fine glass bar via glue. Diffraction intensity data were collected on a Bruker Apex II diffractometer equipped with a CCD bidimensional detector with the graphite-monochromated Mo Kα radiation (λ = 0.71073 Å) at 296 K. The absorption correction was using the SADABS program.[71] Direct methods were used to solve their structures and locate the heavy atoms using the SHELXTL-97 program package.[72,73] The remaining atoms were found from the consecutive full-matrix least-squares refinements on $F^2$ and Fourier syntheses. No hydrogen atoms associated with water molecules were located from the difference Fourier map. Non-hydrogen atoms were

## Table 1. Crystallographic Data and Structure Refinement for 1–13

| | 1 | 2 | 3 | 4 | 5 | 6 |
|---|---|---|---|---|---|---|
| empirical formula | $C_{42}H_{113}N_{13}O_{93}Gd_2P_2W_{17}$ | $C_{42}H_{113}N_{13}O_{93}Tb_2\,P_2W_{17}$ | $C_{42}H_{113}N_{13}O_{93}Dy_2P_2W_{17}$ | $C_{42}H_{113}N_{13}O_{93}Ho_2P_2W_{17}$ | $C_{42}H_{113}N_{13}O_{93}Er_2P_2W_{17}$ | $C_{42}H_{113}N_{13}O_{93}Tm_2P_2W_{17}$ |
| fw | 5790.11 | 5793.45 | 5800.61 | 5805.47 | 5810.17 | 5813.70 |
| crystal system | triclinic | triclinic | triclinic | triclinic | triclinic | triclinic |
| space group | $P\bar{1}$ | $P\bar{1}$ | $P\bar{1}$ | $P\bar{1}$ | $P\bar{1}$ | $P\bar{1}$ |
| a, Å | 14.4071(19) | 14.4184(13) | 14.3581(12) | 14.4058(9) | 14.4029(8) | 14.4223(17) |
| b, Å | 17.488(2) | 17.4770(15) | 17.4154(14) | 19.2919(8) | 17.4116(10) | 17.513(2) |
| c, Å | 23.321(3) | 23.332(2) | 23.1248(19) | 23.3687(15) | 23.2757(13) | 23.295(3) |
| α, deg | 101.074(2) | 101.018(2) | 100.9080(10) | 101.1260(10) | 101.1610(10) | 101.151(2) |
| β, deg | 97.414(2) | 97.397(2) | 97.3480(10) | 97.5370(10) | 97.5480(10) | 97.481(2) |
| γ, deg | 101.596(2) | 101.616(2) | 101.9870(10) | 101.6470(10) | 101.5790(10) | 101.689(2) |
| V, Å⁻³ | 5562.3(13) | 5566.8(9) | 5469.3(8) | 5529.5(6) | 5521.4(5) | 5564.5(11) |
| Z | 2 | 2 | 2 | 2 | 2 | 2 |
| μ, mm⁻¹ | 18.821 | 18.885 | 19.295 | 19.164 | 19.280 | 19.217 |
| F(000) | 5232 | 5236 | 5280 | 5244 | 5246 | 5252 |
| T, K | 296(2) | 296(2) | 296(2) | 296(2) | 296(2) | 296(2) |
| limiting indices | $-11 \le h \le 17$ $-20 \le k \le 20$ $-27 \le l \le 27$ | $-16 \le h \le 17$ $-20 \le k \le 20$ $-27 \le l \le 27$ | $-17 \le h \le 17$ $-20 \le k \le 20$ $-25 \le l \le 27$ | $-17 \le h \le 13$ $-20 \le k \le 20$ $-26 \le l \le 27$ | $-10 \le h \le 17$ $-20 \le k \le 20$ $-27 \le l \le 27$ | $-16 \le h \le 17$ $-20 \le k \le 20$ $-15 \le l \le 27$ |
| no. of reflections collected | 28057 | 28424 | 28043 | 28398 | 28355 | 28179 |
| no. of independent reflections | 19346 | 19425 | 19074 | 19318 | 19314 | 19425 |
| $R_{int}$ | 0.0600 | 0.0382 | 0.0358 | 0.0346 | 0.0437 | 0.0408 |
| data/restraints/parameters | 19346/136/1287 | 19425/43/1288 | 19074/37/1288 | 19318/37/1294 | 19314/105/1294 | 19425/143/1286 |
| goodness-of-fit on $F^2$ | 1.042 | 1.058 | 0.936 | 1.064 | 1.035 | 1.080 |
| final R indices $[I > 2\sigma(I)]$ | $R_1 = 0.0693$ $wR_2 = 0.1740$ | $R_1 = 0.0508$ $wR_2 = 0.1326$ | $R_1 = 0.0461$ $wR_2 = 0.1221$ | $R_1 = 0.0437$ $wR_2 = 0.1160$ | $R_1 = 0.0507$ $wR_2 = 0.1393$ | $R_1 = 0.0606$ $wR_2 = 0.1510$ |
| R indices (all data) | $R_1 = 0.1015$ $wR_2 = 0.1894$ | $R_1 = 0.0745$ $wR_2 = 0.1427$ | $R_1 = 0.0652$ $wR_2 = 0.1309$ | $R_1 = 0.0592$ $wR_2 = 0.1227$ | $R_1 = 0.0709$ $wR_2 = 0.1559$ | $R_1 = 0.0867$ $wR_2 = 0.1619$ |

| | 7 | 8 | 9 | 10 | 11 | 12 | 13 |
|---|---|---|---|---|---|---|---|
| empirical formula | $C_{42}H_{113}N_{13}O_{93}Yb_2P_2W_{17}$ | $C_{42}H_{113}N_{13}O_{93}Y_2P_2W_{17}$ | $C_{30}H_{150}N_{16}O_{159}Ho_2P_4W_{34}$ | $C_{30}H_{150}N_{16}O_{159}Er_2P_4W_{34}$ | $C_{30}H_{150}N_{16}O_{159}Tm_2P_4W_{34}$ | $C_{30}H_{150}N_{16}O_{159}Yb_2P_4W_{34}$ | $C_{30}H_{150}N_{16}O_{159}Y_2P_4W_{34}$ |
| fw | 5821.69 | 5653.42 | 9983.84 | 9988.51 | 9991.86 | 10000.08 | 9832.81 |
| crystal system | triclinic | triclinic | monoclinic | monoclinic | monoclinic | monoclinic | monoclinic |
| space group | $P\bar{1}$ | $P\bar{1}$ | $C2/c$ | $C2/c$ | $C2/c$ | $C2/c$ | $C2/c$ |
| a, Å | 14.7560(9) | 14.430(2) | 28.786(2) | 28.7954(13) | 28.778(2) | 28.777(3) | 28.814(2) |
| b, Å | 17.3360(11) | 17.444(3) | 26.3949(18) | 26.4250(13) | 26.420(2) | 26.415(3) | 26.428(2) |
| c, Å | 21.4919(14) | 23.343(4) | 25.9965(18) | 26.0094(12) | 25.9506(19) | 25.967(3) | 26.054(2) |
| α, deg | 98.2970(10) | 101.129(2) | 90 | 90 | 90 | 90 | 90 |
| β, deg | 97.3000(10) | 97.439(3) | 119.8890(10) | 119.8560(10) | 119.9270(10) | 119.8710(2) | 119.8690(10) |
| γ, deg | 101.4080(10) | 101.407(2) | 90 | 90 | 90 | 90 | 90 |
| V, Å⁻³ | 5263.7(6) | 5565.3(14) | 17125(2) | 17164.3(14) | 17099(2) | 17117(3) | 17205(3) |
| Z | 2 | 2 | 4 | 4 | 4 | 4 | 4 |
| μ, mm⁻¹ | 20.406 | 18.668 | 23.800 | 23.8002 | 23.949 | 23.980 | 23.448 |
| F(000) | 5254 | 5132 | 17692 | 17700 | 17708 | 17716 | 17468 |
| T, K | 296(2) | 296(2) | 296(2) | 296(2) | 296(2) | 296(2) | 296(2) |

**Table 1. continued**

| | 7 | 8 | 9 | 10 | 11 | 12 | 13 |
|---|---|---|---|---|---|---|---|
| limiting indices | $-17 \leq h \leq 12$ | $-15 \leq h \leq 17$ | $-34 \leq h \leq 33$ | $-18 \leq h \leq 34$ | $-32 \leq h \leq 34$ | $-34 \leq h \leq 34$ | $-25 \leq h \leq 34$ |
| | $-20 \leq k \leq 20$ | $-20 \leq k \leq 20$ | $-31 \leq k \leq 14$ | $-30 \leq k \leq 31$ | $-31 \leq k \leq 31$ | $-24 \leq k \leq 31$ | $-31 \leq k \leq 31$ |
| | $-25 \leq l \leq 25$ | $-27 \leq l \leq 22$ | $-30 \leq l \leq 30$ | $-30 \leq l \leq 27$ | $-30 \leq l \leq 15$ | $-30 \leq l \leq 30$ | $-30 \leq l \leq 25$ |
| no. of reflections collected | 27019 | 28524 | 42978 | 43341 | 43564 | 43111 | 43652 |
| no. of independent reflections | 18393 | 19429 | 14978 | 15100 | 15006 | 15008 | 15112 |
| $R_{int}$ | 0.0370 | 0.0428 | 0.0757 | 0.0692 | 0.0710 | 0.0806 | 0.0590 |
| data/restraints/parameters | 18393/37/1361 | 19429/136/1271 | 14978/48/904 | 15100/30/902 | 15006/20/901 | 15008/146/905 | 15112/6/904 |
| goodness-of-fit on $F^2$ | 1.036 | 0.976 | 1.060 | 1.049 | 1.010 | 1.065 | 1.073 |
| final R indices [$I > 2\sigma(I)$] | $R_1 = 0.0472$ | $R_1 = 0.0523$ | $R_1 = 0.0481$ | $R_1 = 0.0496$ | $R_1 = 0.0510$ | $R_1 = 0.0604$ | $R_1 = 0.0458$ |
| | $wR_2 = 0.1020$ | $wR_2 = 0.1327$ | $wR_2 = 0.1150$ | $wR_2 = 0.1286$ | $wR_2 = 0.1253$ | $wR_2 = 0.1557$ | $wR_2 = 0.1089$ |
| R indices (all data) | $R_1 = 0.0782$ | $R_1 = 0.0844$ | $R_1 = 0.0736$ | $R_1 = 0.0897$ | $R_1 = 0.0811$ | $R_1 = 0.0941$ | $R_1 = 0.0726$ |
| | $wR_2 = 0.1108$ | $wR_2 = 0.1459$ | $wR_2 = 0.1245$ | $wR_2 = 0.1479$ | $wR_2 = 0.1732$ | $wR_2 = 0.1700$ | $wR_2 = 0.1176$ |
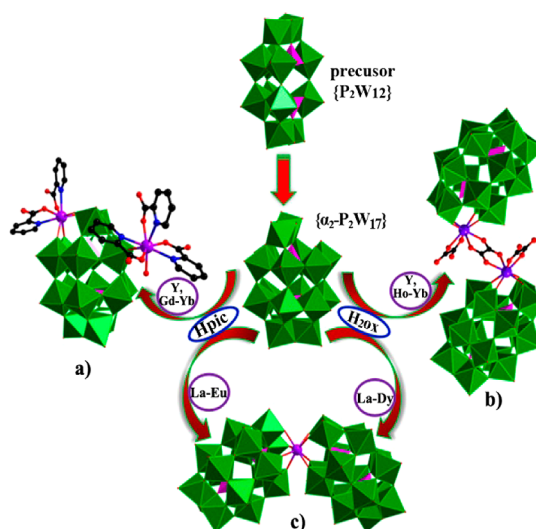


**Figure 1.** Schematic formation processes of **1−8** and **9−13**. (a) The $\{[RE(H_2O)(Hpic)_3][RE(Hpic)_2(\alpha_2\text{-}P_2W_{17}O_{61})]\}^{4-}$ polyoxoanion in **1−8**. (b) The $[RE_2(H_2ox)_2(ox)(\alpha_2\text{-}P_2W_{17}O_{61})_2]^{16-}$ polyoxoanion in **9−13**. (c) The $\lambda$-shaped $[RE(P_2W_{17}O_{61})_2]^{17-}$ polyoxoanion. Color codes: $\{WO_6\}$ octahedra, green; $\{PO_4\}$ tetrahedra, pink; RE, violet; O, red; C, black; N, blue. Lattice water molecules, dissociate $[Hdap]^+$, $[H_2dap]^{2+}$ cations, and hydrogen atoms are omitted for clarity.

refined anisotropically except for some oxygen and water molecules. For **9−13**, two countercations $[H_2dap]^{2+}$ are found from full-matrix least-squares refinements. According to the charge-balance consideration and the experimental results of elemental analyses and TG analyses of **9−13**, another six $[H_2dap]^{2+}$ cations are directly added to each formula, which are in good agreement with the existence of large solvent accessible voids in the check cif reports of their crystal structures. This phenomenon is often encountered in the structural determinations of POMs.[64,74,75] Crystallographic data and structure refinements for **1−8** and **9−13** are demonstrated in Table 1.

## RESULTS AND DISCUSSION

**Synthesis.** In the past decade, some polynuclear TM[12,13] or RE[14] substituted POMs with various organic ligands have been made, and many of them are synthesized at comparatively low pH values. When the pH value of the assembly system stays at a high level, it is extremely difficult to prepare them because amorphous precipitation phases rather than crystals often are obtained as the final products especially for the case in the presence of organoamines. Therefore, the hydrothermal method combined with the relatively high pH value may be an appropriate option to obtain the crystal phases. The volatile $\{P_2W_{12}\}$ precursor can transform to dimeric $\{P_4W_{24}\}$,[58] trimeric $\{P_6W_{36}\}$,[59−62] tetrameric $\{P_8W_{48}\}$,[63,64] tetravacant $\{P_2W_{14}\}$,[65,66] or monovacant $\{P_2W_{17}\}$[67,68] under different reaction conditions. It is well-known that the optimal stability of the $[\alpha_2\text{-}P_2W_{17}O_{61}]^{10-}$ isomer is in the pH range of 5−6, which also plays a key role in the formation of $\alpha_2$-isomer. In the lower pH range of 4−5, it will be isomerized to $[\alpha_1\text{-}P_2W_{17}O_{61}]^{10-}$.[76] When the pH becomes much lower, it will be converted into $[\alpha\text{-}P_2W_{18}O_{62}]^{6-}$.[77] On the basis of the assembly system including the $\{P_2W_{12}\}$ precursor, RE cations, Hpic, and dap under hydrothermal environments in the pH range of 5−6, we successfully obtained a class of Hpic-decorated monovacant RE-substituted Dawson-type phosphotungstate monomers $[Hdap]_4[RE(H_2O)(Hpic)_3][RE(Hpic)_2(\alpha_2\text{-}P_2W_{17}O_{61})]\cdot21H_2O$ [RE = $Gd^{III}$ (**1**), $Tb^{III}$ (**2**), $Dy^{III}$ (**3**), $Ho^{III}$ (**4**), $Er^{III}$ (**5**), $Tm^{III}$ (**6**), $Yb^{III}$ (**7**), $Y^{III}$ (**8**)] (Figure 1). In this system, when RE cations were replaced by $La^{III}$−$Eu^{III}$ cations,

the thin strip-shape crystals of $\lambda$-configuration RESPMs [RE(P$_2$-W$_{17}$O$_{61}$)$_2$]$^{17-}$ were isolated.[44] When Hpic was replaced by oxalate acid in the reaction system, it is amazing that a series of oxalate-decorated monolacunary RE-substituted Dawson-type phosphotungstate dimers [H$_2$dap]$_7$H$_2$[RE$_2$(H$_2$ox)$_2$(ox)($\alpha_2$-P$_2$W$_{17}$-O$_{61}$)$_2$]·25H$_2$O [RE = Ho$^{III}$ (**9**), Er$^{III}$ (**10**), Tm$^{III}$ (**11**), Yb$^{III}$ (**12**), Y$^{III}$ (**13**)] were separated; however, other RE cations were employed under similar environments, and amorphous precipitation phases were afforded, which does not allow us to determine their structures. Obviously, dap played two roles in the preparations of **1**−**13**: (1) dap is alkaline and can be used to increase the pH value of the reaction system; (2) the diprotonated [H$_2$dap]$^{2+}$ cations can serve as the counterions to balance the charge of the resulting products and further enhance the chemical stability of the desired products. In addition, the [H$_2$P$_2$W$_{12}$O$_{48}$]$^{12-}$ precursor was transformed to the [P$_2$W$_{17}$O$_{61}$]$^{10-}$ fragment in the formation of **1**−**13**. When the [P$_2$W$_{17}$O$_{61}$]$^{10-}$ precursor was the starting material under the similar conditions, paralleling experimental results indicated that we failed to obtain **1**−**13**.

**Structural Description.** X-ray single-crystal diffraction shows that **1**−**8** crystallize in the triclinic space group $P\bar{1}$ and **9**−**13** belong to the monoclinic space group $C2/c$. We have compared powder X-ray diffraction (PXRD) patterns of **2**, **3**, **4**, **5**, **6**, **7**, **10**, and **12** with their corresponding simulated XRD patterns from single-crystal X-ray diffraction (Figure S2, Supporting Information). Apparently, all the experiment PXRD patterns are very consistent with their simulated XRD patterns, which indicates that the targeted samples used for the property measurements are pure. The bond valence sum (BVS) calculations indicate that all P, W, and Er centers are +5, +6, and +3 oxidation states,[78] respectively (Tables S1 and S2, Supporting Information).

The molecular unit of isostructural **1**−**8** consists of a RE-Hpic-decorated monovacant Dawson-type phosphotungstate {[RE(H$_2$O)(Hpic)$_3$][RE(Hpic)$_2$($\alpha_2$-P$_2$W$_{17}$O$_{61}$)]}$^{4-}$ [RE = Gd$^{III}$ (**1**), Tb$^{III}$ (**2**), Dy$^{III}$ (**3**), Ho$^{III}$ (**4**), Er$^{III}$ (**5**), Tm$^{III}$ (**6**), Yb$^{III}$ (**7**), Y$^{III}$ (**8**)] hybrid polyoxoanion, four monoprotonated [Hdap]$^+$ countercations as well as 20 one lattice water molecules (Figure 2a). Herein, only the crystal structure of **5** is intensively described. The monovacant Dawson-type phosphotungstate hybrid polyoxoanion of **5** {[Er(H$_2$O)-(Hpic)$_3$][Er(Hpic)$_2$($\alpha_2$-P$_2$W$_{17}$O$_{61}$)]}$^{4-}$ (Figure 2b) is composed of a di-Hpic-chelating [Er1(Hpic)$_2$]$^{3+}$ cation (Figure 2c), a tri-Hpic-chelating [Er2(H$_2$O)(Hpic)$_3$]$^{3+}$ cation (Figure 2d) and a monovacant Dawson-type [$\alpha_2$-P$_2$W$_{17}$O$_{61}$]$^{10-}$ fragment (Figure 2e). Apparently, the [$\alpha_2$-P$_2$W$_{17}$O$_{61}$]$^{10-}$ fragment can be seen as a derivative from the self-decomposition and reassembly of the starting material [H$_2$P$_2$W$_{12}$O$_{48}$]$^{12-}$ during the course of reaction (Figure 2f). As far as we know, the hexavacant [H$_2$P$_2$W$_{12}$O$_{48}$]$^{12-}$ precursor is actually metastable in aqueous solution and can easily transform into other several vacant Dawson-type building blocks, which provides a large amount of possibilities for inlaying addition metal ions. As you can see, the [Er1(Hpic)$_2$]$^{3+}$ cation is incorporated into the defect site of the [$\alpha_2$-P$_2$W$_{17}$O$_{61}$]$^{10-}$ fragment and bonds with the four exposed oxygen atoms (O29, O41, O51, and O59), constructing a mono-RE substituted Dawson-type phosphotungstate [Er(Hpic)$_2$($\alpha_2$-P$_2$W$_{17}$O$_{61}$)]}$^{7-}$ subunit.

Thereinto, the eight-coordinate Er1$^{3+}$ cation is coordinated by two O atoms (O69, O70) [Er−O: 2.284(12)−2.362(14) Å] and two N atoms (N1, N2) [Er−N: 2.510(17)−2.513(18) Å] from two Hpic ligands, and four O atoms (O29, O41,



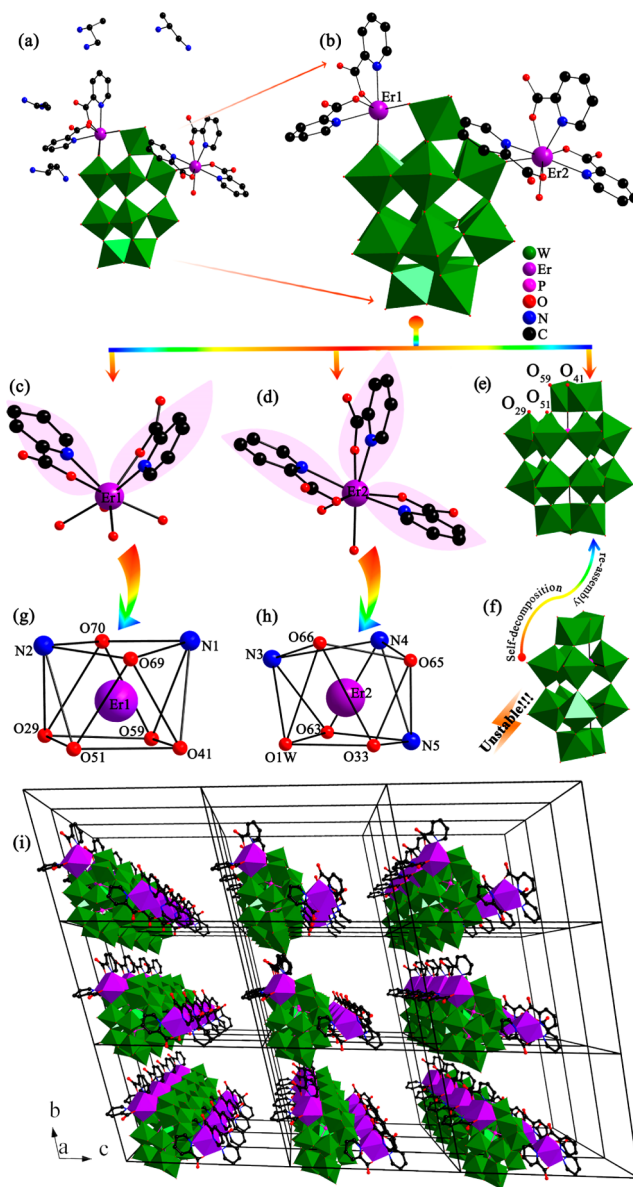**Figure 2.** (a) View of the molecular unit of **1**−**8**. (b) The monovacant Dawson-type phosphotungstate hybrid {[Er(H$_2$O)-(Hpic)$_3$][Er-(Hpic)$_2$($\alpha_2$-P$_2$W$_{17}$O$_{61}$)]}$^{4-}$ polyoxoanion in **5**. (c) The [Er1(Hpic)$_2$]$^{3+}$ cation in **5**. (d) The [Er2(H$_2$O)(Hpic)$_3$]$^{3+}$ cation in **5**. (e) The [$\alpha_2$-P$_2$W$_{17}$O$_{61}$]$^{10-}$ fragment in **5**. (f) The hexavacant [H$_2$P$_2$W$_{12}$O$_{48}$]$^{12-}$ precursor. (g) The octa-coordinate distorted square antiprismatic geometry of the Er1$^{3+}$ ion in **5**. (h) The octa-coordinate distorted square antiprism of the Er2$^{3+}$ ion in **5**. (i) The packing arrangement of **5**. Lattice water molecules and dissociate [Hdap]$^+$ cations are omitted for clarity.

O51, O59) [Er−O: 2.266(11)−2.321(11) Å] from the monovacant [$\alpha_2$-P$_2$W$_{17}$O$_{61}$]$^{10-}$ fragment and exhibits a distorted square antiprism geometry (Figure 2g). Intriguingly, the layout of Hpic1 and Hpic2 (according to N1 and N2, respectively) in [Er1(Hpic)$_2$]$^{3+}$ cation are aligned in the reverse motif with the dihedral angle of 103.98° for ∠Hpic1−Er1−Hpic2, which may be owing to the stereohindrance effect. As for the tri-Hpic-chelating [Er2(H$_2$O)(Hpic)$_3$]$^{3+}$ cation (Figure 2d), the mono-RE substituted Dawson-type [Er(Hpic)$_2$($\alpha_2$-P$_2$W$_{17}$O$_{61}$)]}$^{7-}$ subunit acting as a monodentate ligand coordinates to the [Er2-(H$_2$O)(Hpic)$_3$]$^{3+}$ cation through a terminal oxygen atom from the equatorial tungsten center. The coordination sphere of the
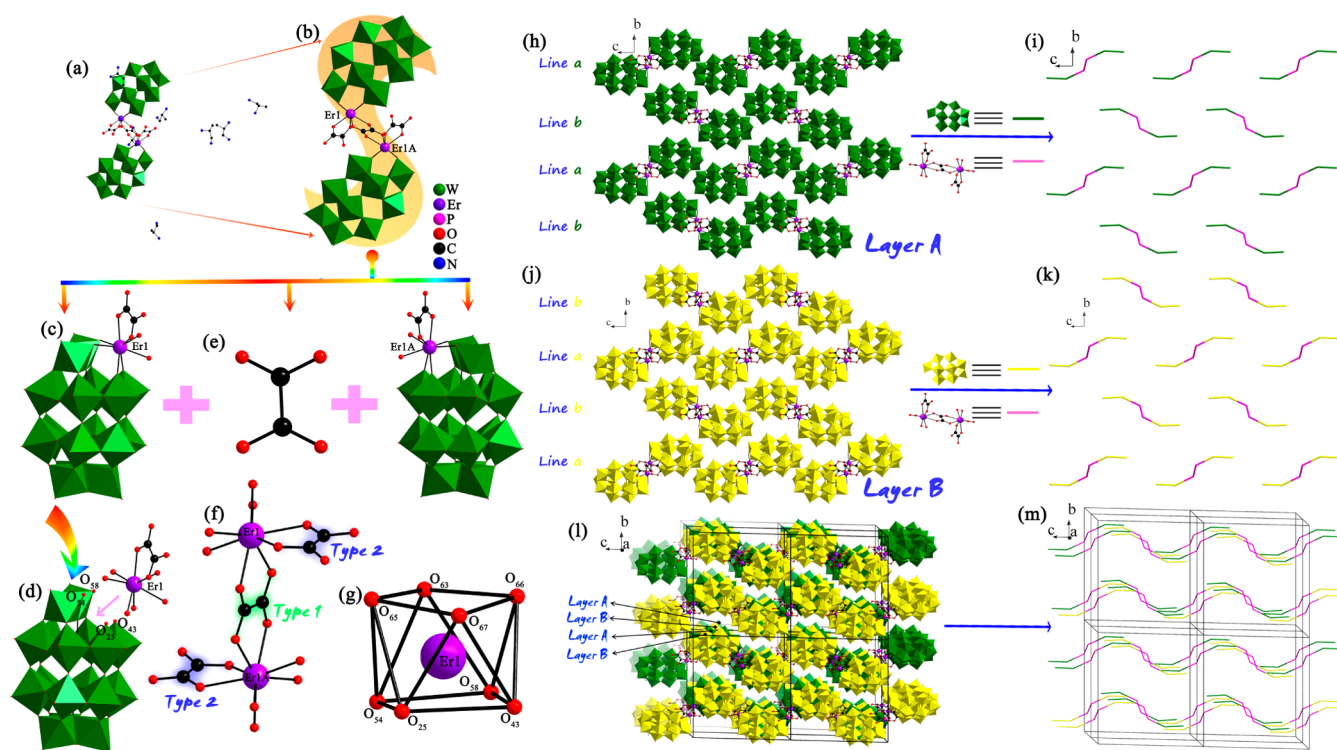
**Figure 3.** (a) View of the molecular unit of **9−13**. (b) The double-Dowson-type $[Er_2(H_2ox)_2(ox)(\alpha_2\text{-}P_2W_{17}O_{61})_2]^{16-}$ polyoxoanion in **10**. The atom with the suffix A is generated by the symmetry operation where A: $-x - 0.5, -y + 1.5, -z + 1$. (c) The mono-RE substituted Dawson-type phosphotungstate $[Er(H_2ox)(\alpha_2\text{-}PW_{17}O_{61})]^{7-}$ subunit in **10**. (d) The $[\alpha_2\text{-}P_2W_{17}O_{61}]^{10-}$ fragment in **10**. (e) The bridging $ox^{2-}$ group in **10**. (f) The two kinds of $H_2ox$ functionalized ligands in **10**. (g) The octa-coordinate distorted square antiprismatic geometry of the $Er1^{3+}$ cation in **10**. (h) The 2-D layer (Layer A) with two types of spatial orientations for polyoxoanions in **10**. (i) The simplified Layer A in **10**. (j) The 2-D layer (Layer B) with two types of spatial orientations for polyoxoanions in **10**. (k) The simplified Layer B in **10**. (l) The 3-D packing architecture with an organized − A− B−A−B− array in **10**. (m) The simplified 3-D packing architecture of **10**. Lattice water molecules and dissociate $[H_2dap]^{2+}$ cations are omitted for clarity.

$Er2^{3+}$ cation is completed by one O atom [Er−O33:2.315(11) Å] from Dawson-type $[Er(Hpic)_2(\alpha_2\text{-}P_2W_{17}O_{61})]\}^{7-}$ subunit, one O atom [Er−O1W: 2.358(12) Å] from a coordinate water molecule, another three O (O63, O65, O66) atoms [Er−O: 2.295(12)−2.330(13) Å] and three N (N5, N4, N3) atoms [Er−N: 2.492(14)−2.513(16) Å] from three Hpic ligands, which reveals the distorted square antiprismatic coordination environment (Figure 2h). Analogously, in order to reduce the steric hindrance, Hpic3, Hpic4 and Hpic5 (in accord with N5, N3, N4, respectively) ligands are arranged with different orientations with the dihedral angle of 77.55°, 81.15°, and 138.05° for ∠Hpic4−Er2−Hpic5, ∠Hpic4−Er2−Hpic3, and ∠Hpic3−Er2−Hpic5, respectively. What is more, it is noteworthy that every Hpic ligand in $[Er1(Hpic)_2]^{3+}$ and $[Er2-(H_2O)(Hpic)_3]^{3+}$ cations chelates with $Er^{3+}$ centers through N and O linkers forming a stable five-member ring, which is conducive to consolidate the whole structure of **5**. Attractively, neighboring $\{[Er(H_2O)(Hpic)_3][Er(Hpic)_2(\alpha_2\text{-}P_2W_{17}O_{61})]\}^{4-}$ polyoxoanions are aligned in a parallel mode in the 3-D packing (Figure 2f), in which the discrete $[Hdap]^+$ cations and solvent water molecules are filled accompanying electrostatic forces between $[Hdap]^+$ cations and polyoxoanions as well as the abundant hydrogen bonding interactions with N−H···O distances of 2.68(4)−3.35(3) Å, N−H···N distances of 2.36(3) Å, O−H···O distances of 2.657(17)−3.21(4) Å, and O−H···N distances of 3.06(3) Å (Figure S3, Supporting Information).

The molecule structure of isostructural **9−13** contains one RE- ox-bridging monovacant Dawson-type phosphotungstate dimeric polyoxoanion $[RE_2(H_2ox)_2(ox)(\alpha_2\text{-}P_2W_{17}O_{61})_2]^{16-}$, 8 discrete diprotonated $[H_2dap]^{2+}$ cations, 2 $H^+$ protons, and 25 lattice water molecules (Figure 3a). Therefore, only **10** is taken as an example to describe in detail. The main polyoxoanion skeleton of **10** is made up of two mono-RE substituted Dawson-type phosphotungstate $[Er(H_2ox)(\alpha_2\text{-}PW_{17}O_{61})]^{7-}$ units linked together through an $ox^{2-}$ bridge, which displays an S-shaped structure (Figure 3b). Similarly to the $[RE-(Hpic)_2(\alpha_2\text{-}P_2W_{17}O_{61})]\}^{7-}$ subunit in **1−8**, each $[\alpha_2\text{-}P_2W_{17}O_{61}]^{10-}$ fragment, derived from the parent $[H_2P_2W_{12}O_{48}]^{12-}$ fragment, is incorporated by an additional $[Er1H_2ox]^{3+}$ electrophile through four Er−O(W) bonds, giving rise to the mono-RE substituted Dawson-type $[RE(H_2ox)(\alpha_2\text{-}P_2W_{17}O_{61})]^{7-}$ subunit (Figure 3c,d). Then, two such subunits are combined by the coordination of one $ox^{2-}$ bridging moiety (Figure 3e) to two $Er^{3+}$ centers with a trans arrangement, forming an intriguing double-Dawson-type $[Er_2(H_2ox)_2(ox)-(\alpha_2\text{-}P_2W_{17}O_{61})_2]^{16-}$ polyoxoanion. Thus, the skeleton of such dimeric polyoxoanion is centrosymmetric and the symmetric center is located at the center of the $ox^{2-}$ bridging moiety. Notably, three $H_2ox$ ligands in this dimeric polyoxoanion simultaneously exhibit two types of functions, one of them acts as a chelating group to bridge two mono-RE substituted POM subuits together (namely, type 1), and the remaining two $H_2ox$ ligands hang at two $Er1^{3+}$ centers constituting two pendant groups (namely, type 2), respectively (Figure 3f). As far as we

know, this phenomenon is not common in POM chemistry. As shown in Figure 3g, each eight-coordinate $Er1^{3+}$ cation also displays the distorted square antiprismatic geometry, bonding to four O atoms (O25, O43, O54, O58) [Er−O: 2.290(12)− 2.349(14) Å] located on the vacant site of the $[\alpha_2\text{-}P_2W_{17}O_{61}]^{10-}$ fragment, two O atoms (O63, O65) [Er−O: 2.317(16)− 2.413(15) Å] from the decorated $H_2ox$ ligand, and another two O atoms (O66, O67) [Er−O: 2.332(13)− 2.417(15) Å] belonging to the bridging $ox^{2-}$ ligand. It is obvious that O25, O43, O54, and O58 atoms constitute one bottom plane while O63, O65, O66, and O67 atoms define the other bottom plane. The average deviations from their least-squares planes of the two bottom planes of the square antiprism are 0.0297 and 0.0599 Å, respectively. The dihedral angle for two bottom planes is 3.6°. The distances between the $Er1^{3+}$ cation and two bottom planes are respectively 1.1610 and 1.3980 Å, and the O−Er−O bond angles are in the range of 67.5(6)−147.6(5) °.

Compared with **5**, the space packing for **10** is quite interesting. Viewed along the *a* axis, the $[Er_2(H_2ox)_2(ox)(\alpha_2\text{-}P_2W_{17}O_{61})_2]^{16-}$ polyoxoanions in layer A exhibit two types of spatial orientations (named as line a and line b) and are arranged in the stagger fashion with the −a−b−a−b− pattern (Figure 3h,i). However, behind layer A, the alternative polyoxoanions in layer B display another −b−a−b−a− arrangement mode (Figure 3j,k). Thus, the two closed layers in the crystal lattice of **10** is also staggered and further stacked in parallel down the *a* axis to give an organized −A−B−A−B− array, which is contributed to reduce the steric hindrance as much as possible (Figure 3l,m). Generally, crystal lattices are filled with dap, and water molecules are always accompanied by abundant hydrogen bonding interactions. Therefore, the 3-D supermolecular assembly of **10** (Figure S4, Supporting Information) is formed and enhanced through hydrogen-bonding interactions between O atoms of the $[Er_2(H_2ox)_2(ox)(\alpha_2\text{-}P_2W_{17}O_{61})_2]^{16-}$ polyoxoanions, lattice water molecules and $[H_2dap]^{2+}$ cations with N−H···O distances of 2.78(3)−3.25(2) Å and O−H···O distances of 2.67(5)−3.08(2) Å. As we can see, dimers **9−13** are comparable to the Keggin-type RESPMs $\{[(\alpha\text{-}PW_{11}O_{39})RE(H_2O)]_2(C_2O_4)\}^{10-}$ (RE = $Y^{III}$, $Dy^{III}$, $Ho^{III}$, $Er^{III}$) (**A**) reported by Niu's group.[38] Their common features are that the fundamental polyoxoanion skeletons are constructed from the classical monolacunary POM fragments joined together by the bridging $ox^{2-}$ ligand. The main discrepancies between **A** and **9−13** lie in the following aspects: (i) the POM building blocks of **A** are monolacunary Keggin-type phosphotungstate fragments, whereas the POM building blocks of **9−13** are monolacunary Dawson-type phosphotungstate fragments; (ii) in contrast with **A**, each Dawson-type POM building block in our RESPMs has an amazing pendent $H_2ox$ ligand; (iii) **A** was synthesized in a HAc−NaAc buffer solution while **9−13** were obtained under hydrothermal conditions. Besides, Kortz's group reported an analogous acetate-bridging monolacunary Dawson-type phosphotungstate dimers $[\{La(CH_3COO)(H_2O)_2(\alpha_2\text{-}P_2W_{17}O_{61})\}_2]^{16-}$ (**B**).[52] In comparison with **B**, there are some obvious distinctions: (i) adjacent two RESPM $[RE(H_2C_2O_4)(\alpha_2\text{-}P_2W_{17}O_{61})]^{7-}$ subunits are interconnected by an oxalate ligand in **9−13**, whereas neighboring two RESPM $[La(H_2O)_2(\alpha_2\text{-}P_2W_{17}O_{61})]^{6-}$ moieties in **B** are linked by two acetate bridges; (ii) different from the hydrothermal synthesis for **9−13**, **B** is obtained in the conventional aqueous solution; (iii) the oxalic acid ligands in **9−13** exhibit two kinds of coordination modes (namely, the

suspending-type $H_2C_2O_4$ and the bridging-type $C_2O_4^{2-}$ anion). In contrast, **B** only has the bridging-type carboxylic ligand. Up to now, only one example of oxalate-bridging tetrameric Dawson POM $[\{Yb(P_2W_{17}O_{61})\}_4(C_2O_4)_3(H_2O)_4]^{34-}$ (**C**) has been isolated by Mialane et al.[53] Obviously, they are all constructed by the oxalate-bridging RESPMs fragments. Moreover, the major discrepancies are as follows: (i) adjacent dimeric polyoxoanion segments in **C** are further connected by one oxalate ligand forming the tetramer, while the decoration-type $H_2C_2O_4$ attached to dimeric polyoxoanion segments in **9−13** are free, which lays a foundation for further functionalization of carboxylated RESPOMs derivatives; (ii) **9−13** were synthesized by reaction of $[H_2P_2W_{12}O_{48}]^{12-}$ with RE cations in the pH range of 5−6 under hydrothermal environments, whereas **C** was prepared by heating the $[Yb(P_2W_{17}O_{61})]^{7-}$ precursor in a 1 mol $L^{-1}$ $NH_4Cl$ aqueous solution (pH 7) in the presence of oxalic acid.

**Solid-State UV−visible Photoluminescence (PL) Properties of 2, 3, 5, and 10.** The solid photoluminescence properties of **2** and **3** have been measured with their crystalline samples upon photoexcitation at room temperature. For **2**, the obvious emission peaks maxima at 488, 544, 583, and 614 nm (Figure 4a) are the characteristic transitions from the $^5D_4$ excited state of the $Tb^{III}$ ions to ground state $^7F_J$ (J = 6, 5, 4, and 3) manifold, respectively.[79,80] Among them, the $^5D_4 \rightarrow {}^7F_5$ transition appearing at 544 nm is the strongest, leading to a strong green emission for **2**. The excitation spectrum with the peak maximum at 378 nm by monitoring the $Tb^{III}$ emission at 544 nm, which corresponds to the absorption by the f−f electron transitions of $Tb^{III}$ ions (Figure S5a, Supporting Information). In addition, the lifetime decay curve of **2** measured under the strongest emission at 544 nm and the excitation at 378 nm (Figure 4b) can be fitted to a double exponential function $[I = A_1 \exp(-t/\tau) + A_2 \exp(-t/\tau)]$, yielding two pre-exponential factors (A) of 440.51 for $A_1$ and 63.04 for $A_2$, the luminescence lifetimes ($\tau$) of 52.50 μs for $\tau_1$ (45.89%) and 432.46 μs for $\tau_2$ (54.11%) and an agreement factor ($\chi^2$) of 1.299. The average decay time ($\tau^*$ = 258.072 μs) can be determined by the following equation $\tau^* = (A_1\tau_1^2 + A_2\tau_2^2)/(A_1\tau_1 + A_2\tau_2)$ and the average decay time $\tau^*$ can be calculated to 258.072 μs.[81,82] On the basis of the structural description of **2**, two crystallographically unique $Tb^{III}$ ($[Tb1(Hpic)_2]^{3+}$ and $[Tb2(H_2O)(Hpic)_3]^{3+}$) cations exist in the structure of **2**. Although $[Tb1(Hpic)_2]^{3+}$ and $[Tb2(H_2O)(Hpic)_3]^{3+}$ cations inhabit in the distorted square antiprismatic geometry, their coordination environments are different. As is known to all that water ligands normally can quench the fluorescence emission. Thus, it can be conjectured that the long lifetime of 432.46 μs stems from the $[Tb1(Hpic)_2]^{3+}$ cation and the short lifetime of 52.50 μs results from the $[Tb2(H_2O)(Hpic)_3]^{3+}$ cation.

In the case of **3**, three characteristic emission peaks of the $Dy^{3+}$ cations appear at 479, 573, and 660 nm in the emission spectrum recorded under the excitation at 384 nm (Figure 4c). Two weak emission peaks at 479 and 660 nm correspond to the $^4F_{9/2} \rightarrow {}^6H_{15/2}$ and $^4F_{9/2} \rightarrow {}^6H_{11/2}$ transitions, respectively, while the strong emission peak at 573 nm leads to the yellow luminescence (Figure 5), which can be assigned to the $^4F_{9/2} \rightarrow {}^6H_{13/2}$ transition.[83−85] As we know, the $^4F_{9/2} \rightarrow {}^6H_{15/2}$ transition is a magnetic dipole transition, which is always independent with the crystal field strength and coordination environment around the $Dy^{3+}$ ions, whereas the $^4F_{9/2} \rightarrow {}^6H_{13/2}$ transition is an electric dipole transition and hypersensitive to
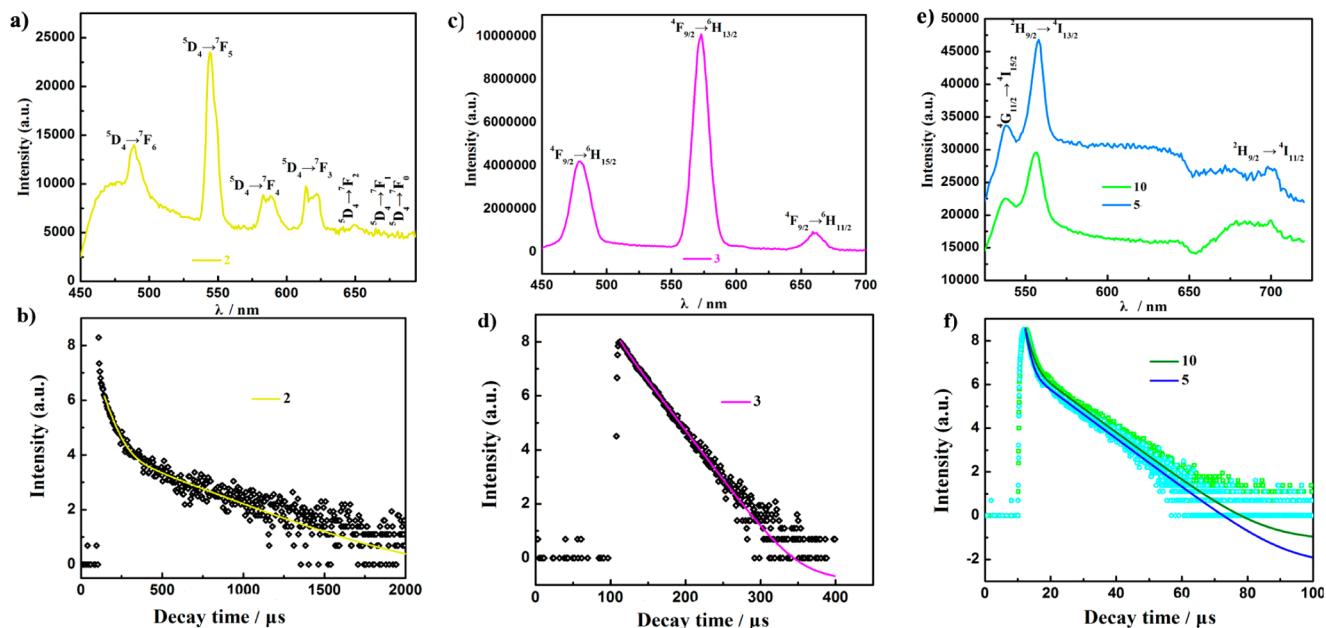
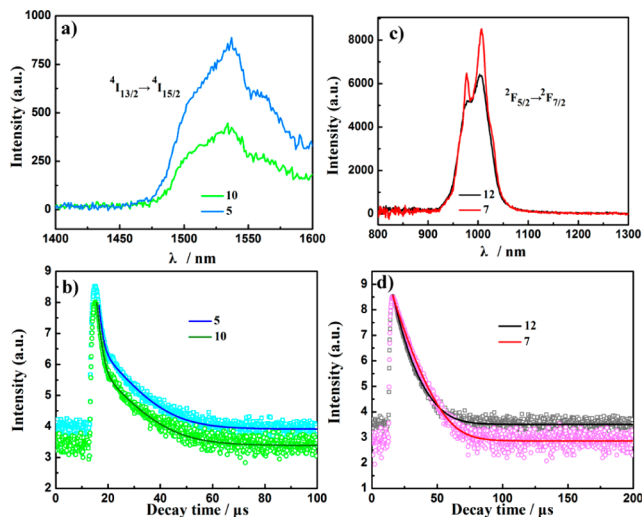**Figure 4.** (a) The emission spectrum of **2** under the excitation at 378 nm at room temperature. (b) The lifetime decay curve of **2** monitored at the emission of 544 nm under the excitation at 378 nm. (c) The emission spectrum of **3** under the excitation at 384 nm. (d) The lifetime decay curve of **3** monitored at the emission of 573 nm under the excitation at 384 nm. (e) The emission spectra of **5** and **10** under the excitation at 380 nm. (f) The lifetime decay curves of **5** and **10** monitored under the excitation at 380 nm and the emission at 556 nm.



**Figure 5.** (a) The NIR emission spectra of **5** and **10** under the excitation at 380 nm at room temperature. (b) The lifetime decay curves of **5** and **10** monitored under the excitation at 380 nm and the emission at 1535 nm. (c) The NIR emission spectra of **7** and **12** under the excitation at 380 nm at room temperature. (d) The lifetime decay curves of **7** and **12** monitored under the excitation at 380 nm and the emission at 1003 nm.

the local environments and the crystal field around the $Dy^{3+}$ ions.[86−89] Obviously, the peak intensity originating from the $^4F_{9/2} \rightarrow {}^6H_{13/2}$ electric dipole transition is much higher than that originating from the $^4F_{9/2} \rightarrow {}^6H_{15/2}$ magnetic dipole transition in the emission spectrum of **3** (Figure 4c), which evidently indicates that the $Dy^{3+}$ ions are located at the low symmetrical environments and agrees with the fact that two crystallographically independent $Dy^{3+}$ ions reside in the severely distorted square antiprismatic geometry in **3**. Moreover, the strong peak at 384 nm and the other three middle peaks at 348, 362, 422 nm (Figure S5b, Supporting Information)

in the excitation spectrum collected by monitoring the Dy(III) emission at 573 nm can be respectively attributed to the $^6H_{15/2} \rightarrow {}^4I_{13/2}$, $^6H_{15/2} \rightarrow {}^6P_{7/2}$, $^6H_{15/2} \rightarrow {}^6P_{5/2}$, and $^6H_{15/2} \rightarrow {}^4G_{11/2}$ transitions, which stems from the absorption by the f−f electron transitions of $Dy^{III}$ ions. Furthermore, the decay curve of **3** has also been examined under the most intense emission at 573 nm and the excitation at 384 nm (Figure 4d), which also abides a second-order exponential function with two pre-exponential factors ($A$) of 411.29 for $A_1$ and 2707.87 for $A_2$, an agreement factor ($\chi^2$) of 1.073 and the fitted luminescence life-times ($\tau$) of 8.61 $\mu$s for $\tau_1$ (4.58%) and 27.24 $\mu$s for $\tau_2$ (95.42%) with the average decay time ($\tau^* = 29.961$ $\mu$s). Similarly, the long lifetime of 27.24 $\mu$s originates from the $[Dy1(Hpic)_2]^{3+}$ cation and the short lifetime of 8.61 $\mu$s results from the $[Dy2(H_2O)(Hpic)_3]^{3+}$ cation.

With regard to **5** and **10**, both exhibit the green fluorescence under the excitation at 380 nm (Figure 4e). Three featured emission bands at 537, 556, and 700 nm correspond to the $^4S_{3/2} \rightarrow {}^4I_{15/2}$, and $^2H_{9/2} \rightarrow {}^4I_{11/2}$ transitions of the $Er^{3+}$ cations, respectively.[90] By monitoring the $^2H_{9/2} \rightarrow {}^4I_{13/2}$ emission at 556 nm, the excitation spectra of **5** and **10** have been collected and display one typical excitation band at 380 nm, which is ascribed to the $^4G_{11/2} \rightarrow {}^4I_{15/2}$ transition of the $Er^{3+}$ cations (Figure S5c, Supporting Information).[91−93] Obviously, the emission intensity of **5** is higher than that of **10**, which suggests that Hpic ligand can more effectively sensitize the emission of the $Er^{3+}$ cations than the oxalic acid ligand. Additionally, the fluorescence decay curves of **5** and **10** have also been measured under their common excitation at 380 nm and their strongest emission at 556 nm (Figure 4f), which can be well fitted to a double exponential function. As for **5**, it yields the pre-exponential factors of 3545.19 for $A_1$ and 602.47 for $A_2$, an agreement factor ($\chi^2$) of 1.270 as well as the fitted luminescence lifetimes of 1.06 $\mu$s for $\tau_1$ (41.49%) and 8.80 $\mu$s for $\tau_2$ (58.51%) with the average decay time ($\tau^* = 5.59$ $\mu$s). With regard to **10**, it affords the pre-exponential factors of 2428.49

for $A_1$ and 351.03 for $A_2$, an agreement factor ($\chi^2$) of 1.116 as well as the fitted luminescence lifetimes of 0.90 $\mu$s for $\tau_1$ (41.01%) and 8.96 $\mu$s for $\tau_2$ (58.99%) and the average decay time ($\tau^* = 5.65$ $\mu$s). Similar to **2** and **3**, in the case of **5**, the long lifetime is derived from the $[Er1(Hpic)_2]^{3+}$ cation and the short lifetime comes from the $[Er2(H_2O)(Hpic)_3]^{3+}$ cation. Notably, different from **2**, **3**, and **5**, there is only one crystallographically independent $Er^{3+}$ cation in **10**; however, it has two decay lifetimes. On the basis of the Yamase and co-workers' results,[94] the ligand to metal O → W charge transfer (LMCT) transitions of W−O skeletons may contribute to the emission behaviors of RESPMs, we measured the emission spectrum and the lifetime decay curve of solid-state $K_{10}[\alpha_2\text{-}P_2W_{17}O_{61}]\cdot20H_2O$ under the same conditions to **10**. As shown in Figure S6a in the Supporting Information, the luminescence spectrum of $K_{10}[\alpha_2\text{-}P_2W_{17}O_{61}]\cdot20H_2O$ really reveals a broad emission band centered at approximately 700 nm, which is induced by the $^3T_{1u} \rightarrow {^1A_{1g}}$ transition derived from the O → W LMCT transitions.[94] Furthermore, in the emission of spectrum of **10**, a weak broad emission band can be clearly seen between 660 and 720 nm, which further certifies that $[\alpha_2\text{-}P_2W_{17}O_{61}]^{10-}$ fragments play a part role in the emission process of **10**. As expected, the decay curve of $K_{10}[\alpha_2\text{-}P_2W_{17}O_{61}]\cdot20H_2O$ obeys the double exponential function with 1.29 $\mu$s for $\tau_1$ (42.87%) and 9.14 $\mu$s for $\tau_2$ (57.13%) (Figure S6b, Table S3, Supporting Information). In conclusion, the emission behavior of **10** is the result of simultaneous actions of the $Er^{3+}$ cations and the $^3T_{1u} \rightarrow {^1A_{1g}}$ transition derived from the O → W LMCT transitions.

The CIE 1931 diagram combining three primary colors has been widely used for determining the emission colors of as-synthesized materials. On the basis of the corresponding photoluminescence spectra of **2**, **3**, **5**, and **10**, their CIE diagram has been drawn (Figure S7, Supporting Information). The CIE chromaticity coordinates $x$ and $y$ are used to distinguish the precise emission colors. The CIE chromaticity for **2**, **3**, **5**, and **10** are determined and are respectively indexed to ($x = 0.318$, $y = 0.413$), ($x = 0.358$, $y = 0.423$), ($x = 0.410$, $y = 0.529$), and ($x = 0.399$, $y = 0.547$). Thus, the whole emissions of four samples are evaluated according to the standard CIE chromaticity diagram, which can be easily observed to be bluish green for **2**, the yellow-green for **3**, and the green for **5** and **10**.

**Solid-State NIR PL Properties of 5, 7, 10, and 12.** The NIR emission spectra of **5**, **10**, **7**, and **12** have been measured at the excitation of 380 nm at room temperature. The characteristic emission bands of $Er^{3+}$ and $Yb^{3+}$ ions respectively appear at 1535 and 1003 nm, which can be assigned to the $^4I_{13/2} \rightarrow {^4I_{15/2}}$ transition of the $Er^{3+}$ ions and the $^2F_{5/2} \rightarrow {^2F_{7/2}}$ transition of the $Yb^{3+}$ ions (Figure 5a,c). Obviously, the emission intensities of **5** and **7** are higher than those of **10** and **12**, which further shows that the 2-picolinic acid ligand can more effectively sensitize the emission of the $Er^{3+}$ cations than oxalic acid ligand. Furthermore, all these NIR decay curves of **5**, **10**, **7**, and **12** can be fitted to the double exponential function. As for **5**, it yields the pre-exponential factors of 2289.14 for $A_1$ and 654.15 for $A_2$, an agreement factor ($\chi^2$) of 1.222 and the fitted luminescence lifetimes of 0.97 $\mu$s for $\tau_1$ (26.92%) and 9.26 $\mu$s for $\tau_2$ (73.08%) with the average decay time $\tau^* = 7.03$ $\mu$s (Figure 5b). With regard to **10**, it affords the pre-exponential factors of 2726.70 for $A_1$ and 360.40 for $A_2$, an agreement factor ($\chi^2$) of 1.234 and the fitted luminescence lifetimes of 1.09 $\mu$s for $\tau_1$ (45.97%) and 9.73 $\mu$s for $\tau_2$ (54.03%) with the average decay time $\tau^* = 5.76$ $\mu$s (Figure 5b). For **7**,

it leads to the pre-exponential factors of 3756.48 for $A_1$ and 1496.94 for $A_2$, an agreement factor ($\chi^2$) of 1.093 and the fitted luminescence lifetimes of 5.35 $\mu$s for $\tau_1$ (57.22%) and 10.03 $\mu$s for $\tau_2$ (42.78%) with the average decay time $\tau^* = 7.35$ $\mu$s (Figure 5d). For **12**, the decay data are the pre-exponential factors of 4291.48 for $A_1$ and 1145.67 for $A_2$, an agreement factor ($\chi^2$) of 1.129 and the fitted luminescence lifetimes of 4.05 $\mu$s for $\tau_1$ (60.68%) and 9.84 $\mu$s for $\tau_2$ (39.32%) with the average decay time $\tau^* = 6.34$ $\mu$s (Figure 5d). Herein, we can conclude that the PL results of $Er^{3+}$ and $Yb^{3+}$ containing RESPMs modified by oxalate acid or 2-picolinic acid show that the PL emission intensity of 2-picolinic-acid-RESPMs are stronger than oxalic acid RESPMs, which should be ascribed to the easier energy transfer from 2-picolinic acid to $Er^{3+}$ or $Yb^{3+}$ ions than that from $H_2C_2O_4$ to $Er^{3+}$ or $Yb^{3+}$ ions, and the energy transfer might originate from the process of $\pi{-}\pi^*$ electronic transition of organic ligands.[92]

**Magnetic Properties.** The direct-current ($dc$) magnetic susceptibility investigation for the crystalline sample of **3** was performed in the temperature range of 2−300 K under an applied field of 1000 Oe using a SQUID magnetometer. The temperature dependence of magnetic susceptibility data for **3** is shown in Figure 6a in the form of $\chi_M$ and $\chi_M T$ versus $T$.
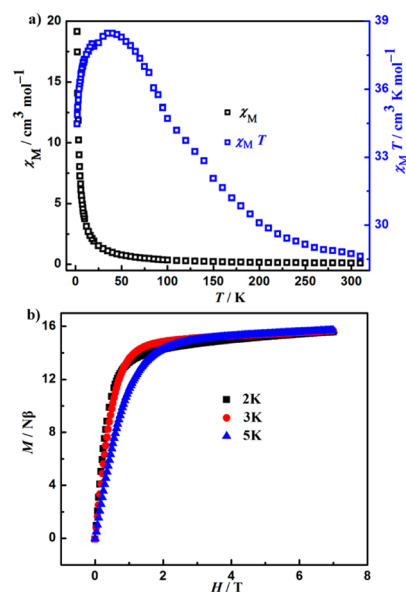


**Figure 6.** (a) Plots of $\chi_M$ and $\chi_M T$ versus $T$ under the applied dc field of 1000 Oe for the powder sample of **3**. (b) Plots of magnetization versus magnetic field for **3** between 2 and 5 K.

At 300 K, the experimental $\chi_M T$ value of 28.62 cm$^3$ K mol$^{-1}$ is in agreement with the theoretical value of 28.34 cm$^3$ K mol$^{-1}$ expected for two noninteracting $Dy^{III}$ ions ($S = 5/2$, $L = 5$, $^6H_{15/2}$, $g = 4/3$).[95] In the beginning, the $\chi_M T$ product increases gradually with decreasing temperature and reaches a round maximum of 38.79 cm$^3$ K mol$^{-1}$ at 41 K, which may indicate that the $S_{Dy} = 5/2$ local spins somewhat tend to align along the same direction.[96] Then, it falls sharply to a minimum of 34.52 cm$^3$ K mol$^{-1}$ at 2 K, which can be ascribed to the thermal depopulation of the $Dy^{III}$ Stark sublevels split by the ligand field and the intermolecular interactions (Figure 6a).[97] Besides, the plot of $\chi_M^{-1}$ versus $T$ in the range of 1.8−300 K conforms to the Curie−Weiss law (Figure S8, Supporting Information), resulting in $C = 29.53$ cm$^3$ mol$^{-1}$ K and $\theta = 4.77$ K. The small

positive $\theta$ value also indicates the weak ferromagnetic interactions between adjacent $Dy^{III}$ ions.

The field dependence of the magnetization for **3** is measured at 2, 3, and 5 K, respectively (Figure 6b). At 2 K, the magnetization exhibits a rapid increase in relatively low magnetic field and then increases gradually to approximately 15.58 N$\beta$ when the magnetic field rises up to 7 T. This unsaturated maximum of 15.58 N$\beta$ at 7 T is lower than the theoretical saturation value of 20 N$\beta$ (Ms/N$\beta$ = 2$g_J$J) for two $Dy^{III}$ ions. The obvious discrepancy between the observed magnetization value and the expected magnetization saturation value may be indicative of the presence of magnetic anisotropy and/or a more likely presence of low lying excited states that are partially (thermally and field-induced).[98,99]

In order to further probe the presence of slow relaxation of magnetization, the alternate-current (*ac*) magnetic susceptibility measurements of **3** have been performed in the temperature range of 2−15 K under a 0, 500, 1000, 2000, 3000, or 4000 Oe dc field and a 3 Oe ac field at 1−999 Hz (Figure 7). Under a zero *dc* field, the out-of-phase susceptibility signals ($\chi''$) exhibit the obvious frequency dependence, indicating the existence of slow relaxation of the magnetization (Figure 7a,b), whereas, due to the quantum tunneling of the magnetization (QTM) decreasing the relaxation barrier,[85] no peak maxima can be observed for the $\chi''$ signals in the low-temperature region, which is very common in the Ln-based SMMs.[100−103] For the purpose of suppressing possible QTM, various static magnetic fields ranging from 500 to 4000 Oe were applied at 2 K to find out the optimum *dc* field (Figure 7c−l).

With increasing the magnetic field from 500 to 3000 Oe, the frequency-dependent $\chi'$ and $\chi''$ susceptibility signals gradually emerge, and the faint peak maxima can be observed, which indicates that the QTM effect has been gradually restrained (Figure 7c−j). When a 4000 Oe *dc* field was used to this system, the frequency-dependent peaks of both $\chi'$ and $\chi''$ at around 4 K can be clearly observed (Figure 7k,l). By means of the frequency dependencies of the *ac* susceptibilities, the magnetization relaxation times ($\tau$) were estimated between 2 and 15 K (Figure S9, Supporting Information). The semicircle shapes of the Cole−Cole diagrams of $\chi''$ vs $\chi'$ were observed in a 4000 Oe dc field between 5.5 and 13 K below 999 Hz (Figure 8a) and fitted to the Debye model with the distribution coefficient $\alpha$ ranging from 0.17 to 0.57, which reveals the presence of a thermally activated relaxation process in the **3** system along with a narrow distribution of relaxation times. The effective relaxation energy barrier has been obtained by fitting $\tau$ values above 4.6 K based on the Arrhenius law [$\tau = \tau_0 \exp(-\Delta E/k_B T)$], giving a calculated $\tau_0$ value of $8.06 \times 10^{-9}$ s and the related energy barrier $\Delta E/k_B$ value of 119.38 K (Figure 8b). Apparently, $\tau_0$ lies in the normal range ($10^{-6}-10^{-12}$ s) of typical SMMs,[95,104] which exhibits that **3** is an SMM.

In addition, the relaxation dynamics have also been investigated. At a sweeping rate of 500 Oe s$^{-1}$, the magnetic hysteresis gradually changes from straight-line to narrow butterfly shape with the low temperature ranging from 15 to 2 K, indicating the dominant aforementioned QTM effect at low temperatures for **3** (Figure 8c). Moreover, as the field
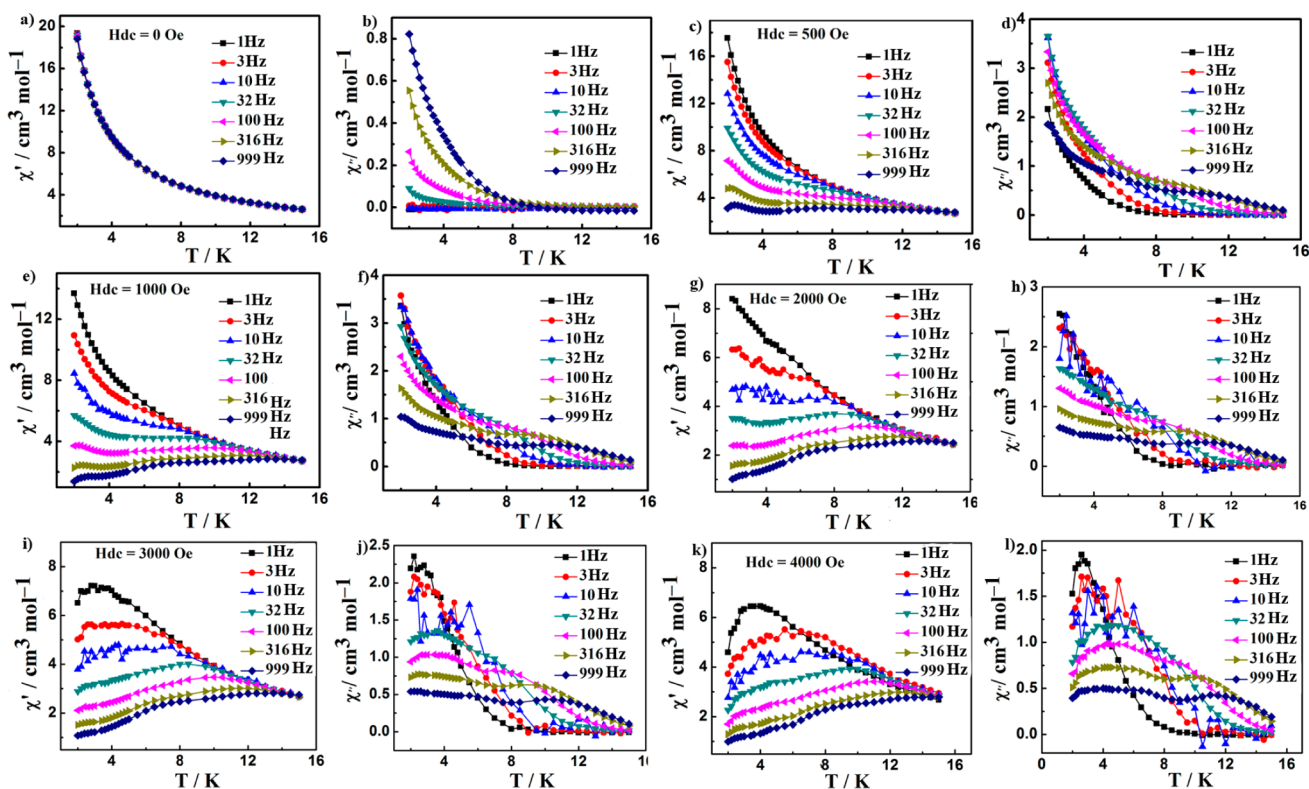


**Figure 7.** (a and b) The *ac* measurements of the in-phase ($\chi'$) and out-of-phase ($\chi''$) signals for **3** under a zero *dc* field. (c and d) The *ac* measurements of the in-phase ($\chi'$) and out-of-phase ($\chi''$) signals for **3** under a 500 Oe dc field. (e and f) The *ac* measurements of the in-phase ($\chi'$) and out-of-phase ($\chi''$) signals for **3** under a 1000 Oe dc field. (g and h) The *ac* measurements of the in-phase ($\chi'$) and out-of-phase ($\chi''$) signals for **3** under a 2000 Oe dc field. (i and j) The *ac* measurements of the in-phase ($\chi'$) and out-of-phase ($\chi''$) signals for **3** under a 3000 Oe dc field. (k and l) The *ac* measurements of the in-phase ($\chi'$) and out-of-phase ($\chi''$) signals for **3** under a 4000 Oe dc field.
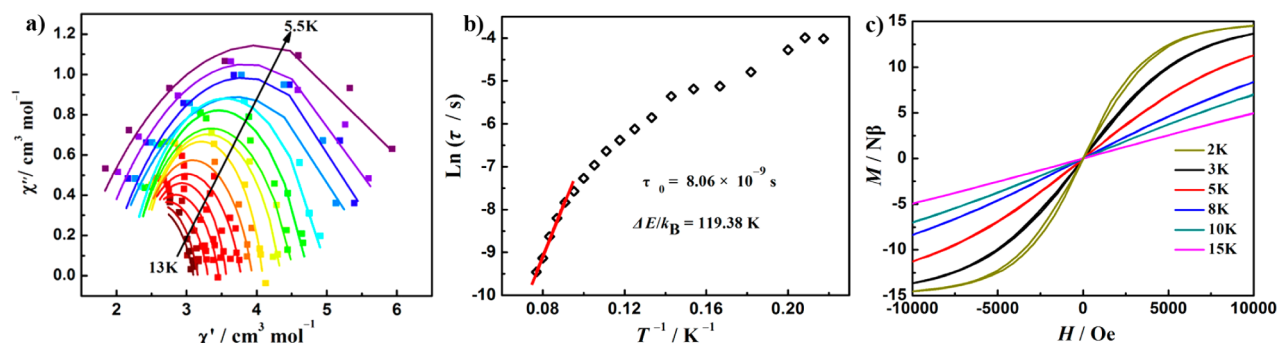
**Figure 8.** (a) Cole−Cole diagrams of **3** with the solid lines represent the best fits to the experimental data. (b) The magnetization relaxation time $\ln(\tau)$ versus $T^{-1}$ plot for **3** represented with the solid red line fits by the Arrhenius equation. (c) Hysteresis loops for **3** measured with temperatures ranging from 2 to 15 K at a sweeping rate of 500 Oe s$^{-1}$.

increases, the loop becomes broader with a maximum emerging at around 4000 Oe, which is consistent with the optimum *dc* field of 4000 Oe. As shown in Figure S10 in the Supporting Information, the hysteresis loop becomes narrower and even almost invisible with the field sweep rate decreasing to 100 Oe s$^{-1}$, which manifests the dynamic behavior of **3**. This dynamic behavior can be usually observed in the related Dy$^{III}$-participated complexes.[105,106] Thus, both the above temperature- and sweep-rate-dependent nature of the hysteresis loop confirm the SMM behavior of **3**.[107]

## CONCLUSIONS

In conclusion, two series of Dawson-type carboxylated monomeric and dimeric RESPMs $\{[RE(H_2O)(Hpic)_3][RE-(Hpic)_2(\alpha_2\text{-}P_2W_{17}O_{61})]\}^{4-}$ [RE = Gd$^{III}$ (**1**), Tb$^{III}$ (**2**), Dy$^{III}$ (**3**), Ho$^{III}$ (**4**), Er$^{III}$ (**5**), Tm$^{III}$ (**6**), Yb$^{III}$ (**7**), Y$^{III}$ (**8**)] and $[RE_2(H_2ox)_2(ox)(\alpha_2\text{-}P_2W_{17}O_{61})_2]^{16-}$ [RE = Ho$^{III}$ (**9**), Er$^{III}$ (**10**), Tm$^{III}$(**11**), Yb$^{III}$ (**12**), Y$^{III}$ (**13**)] have been synthesized by utilizing the hexa-lacunary $\{P_2W_{12}\}$ precursor, carboxylic acid ligands, and rare earth nitrate under mild hydrothermal conditions. The monomeric hybrid polyoxoanion skeleton $\{[RE(H_2O)(Hpic)_3][RE(Hpic)_2(\alpha_2\text{-}P_2W_{17}O_{61})]\}^{4-}$ of **1**−**8** is constituted by a di-Hpic-chelating $[RE(Hpic)_2]^{3+}$ cation, a tri-Hpic-chelating $[RE(H_2O)(Hpic)_3]^{3+}$ cation and a monovacant Dawson-type $[\alpha_2\text{-}P_2W_{17}O_{61}]^{10-}$ fragment, whereas the dimeric Dawson-type hybrid polyoxoanion backbone $[RE_2(H_2ox)_2(ox)(\alpha_2\text{-}P_2W_{17}O_{61})_2]^{16-}$ of **9**−**13** is established by two mono-RE substituted Dawson-type $[RE(H_2ox)(\alpha_2\text{-}PW_{17}O_{61})]^{7-}$ units linked together via an ox$^{2-}$ bridge, demonstrating an S-shaped assembly. The successful preparations of these Dawson-type carboxylated RESPMs not only are conducive to enrich the structure variety of organic−inorganic hybrid RESPMs, but also provide a promising and convenient synthetic approach for designing and assembly novel carboxylated RESPMs with fascinating structures and charming properties. Solid-state UV−visible PL properties of **2**, **3**, **5**, and **10** and solid-state NIR PL properties of **5**, **7**, **10**, and **12** have been investigated. The PL results of Er$^{3+}$ and Yb$^{3+}$ containing RESPMs modified by oxalate acid or 2-picolinic acid indicate that the PL emission intensity of 2-picolinic-acid-RESPMs are stronger than oxalic acid RESPMs, which should be ascribed to the easier energy transfer from 2-picolinic acid to Er$^{3+}$ or Yb$^{3+}$ ions than that from H$_2$C$_2$O$_4$ to Er$^{3+}$ or Yb$^{3+}$ ions, and the energy transfer might be originated from the process of $\pi−\pi^*$ electronic transition of organic ligands. Furthermore, the dynamic magnetic studies display SMM behavior of **3**, which is supported by the fitting results of the Debye model and the Arrhenius law.

In the future, versatile multicarboxylic acid ligands will be introduced to this system to construct novel RESPMs with extended structures. Utilizing a flexible linking fashion and coordination mode of multicarboxylic acid ligands tunes their luminescence and magnetic properties to obtain potential POM-based materials with benign luminescence and magnetic properties.

## ASSOCIATED CONTENT

### ⓢ Supporting Information

The Supporting Information is available free of charge on the ACS Publications website at DOI: 10.1021/acs.cgd.7b00823.

> IR spectra; additional structural figures; PXRD spectra; related PL figures; related magnetic figures; BVS calculations of **5** and **10**; summary of decay lifetimes; selected IR data; TG curves (PDF)

### Accession Codes

CCDC 1555344−1555348 and 1555820−1555827 contain the supplementary crystallographic data for this paper. These data can be obtained free of charge via www.ccdc.cam.ac.uk/data_request/cif, or by emailing data_request@ccdc.cam.ac.uk, or by contacting The Cambridge Crystallographic Data Centre, 12 Union Road, Cambridge CB2 1EZ, UK; fax: +44 1223 336033.

## AUTHOR INFORMATION

**Corresponding Authors**
*E-mail: ljchen@henu.edu.cn.
*E-mail: zhaojunwei@henu.edu.cn. Fax: (+86) 371 23881589.

**ORCID** ⓘ
Jun-Wei Zhao: 0000-0002-7685-1309

**Notes**
The authors declare no competing financial interest.

# ■ REFERENCES

(1) Khenkin, A.; Weiner, M. L.; Wang, Y.; Neumann, R. *J. Am. Chem. Soc.* **2001**, *123*, 8531.

(2) Hill, C. L.; Prosser-McCartha, C. M. *Coord. Chem. Rev.* **1995**, *143*, 407.

(3) Mizuno, N.; Misono, M. *Chem. Rev.* **1998**, *98*, 199.

(4) Yamase, T. *Chem. Rev.* **1998**, *98*, 307.

(5) Hill, C. L. *Angew. Chem., Int. Ed.* **2004**, *43*, 402.

(6) Zhao, J. W.; Li, Y. Z.; Chen, L. J.; Yang, G. Y. *Chem. Commun.* **2016**, *52*, 4418.

(7) Mizuno, N.; Yamaguchi, K.; Kamata, K. *Coord. Chem. Rev.* **2005**, *249*, 1944.

(8) Zhao, J. W.; Zhang, J.; Zheng, S. T.; Yang, G. Y. *Inorg. Chem.* **2007**, *46*, 10944.

(9) Wei, M.; He, C.; Hua, M.; Duan, C. Y.; Li, S.; Meng, Q. J. *J. Am. Chem. Soc.* **2006**, *128*, 13318.

(10) Nsouli, N. H.; Bassil, S. B.; Dickman, M. H.; Kortz, U.; Keita, B.; Nadjo, L. *Inorg. Chem.* **2006**, *45*, 3858.

(11) Hussain, F.; Bassil, B. S.; Kortz, U.; Kholdeeva, O. A.; Timofeeva, M. N.; de Oliveira, P.; Keita, B.; Nadjo, L. *Chem. - Eur. J.* **2007**, *13*, 4733.

(12) Oms, O.; Dolbecq, A.; Mialane, P. *Chem. Soc. Rev.* **2012**, *41*, 7497.

(13) Zheng, S. T.; Yang, G. Y. *Chem. Soc. Rev.* **2012**, *41*, 7623.

(14) Bassil, B. S.; Kortz, U. *Z. Anorg. Allg. Chem.* **2010**, *636*, 2222.

(15) Benelli, C.; Gatteschi, D. *Chem. Rev.* **2002**, *102*, 2369.

(16) Boglio, C.; Lemière, G.; Hasenknopf, B.; Thorimbert, S.; Lacôte, E.; Malacria, M. *Angew. Chem., Int. Ed.* **2006**, *45*, 3324.

(17) Kikukawa, Y.; Yamaguchi, S.; Tsuchida, K.; Nakagawa, Y.; Uehara, K.; Yamaguchi, K.; Mizuno, N. *J. Am. Chem. Soc.* **2008**, *130*, 5472.

(18) El Moll, H. E.; Nohra, B.; Mialane, P.; Marrot, J.; Dupré, N.; Riflade, B.; Malacria, M.; Thorimbert, S.; Hasenknopf, B.; Lacôte, E.; Aparicio, P. A.; López, X.; Poblet, J. M.; Dolbecq, A. *Chem. - Eur. J.* **2011**, *17*, 14129.

(19) Peacock, R. D.; Weakley, T. J. R. *J. Chem. Soc. A* **1971**, 1836.

(20) Fedotov, M.; Pertsikov, B.; Danovich, D. *Polyhedron* **1990**, *9*, 1249.

(21) Pope, M. T. *Compr. Coord. Chem. II* **2003**, *4*, 635.

(22) Hill, C. L. *Compr. Coord. Chem. II* **2003**, *4*, 679.

(23) BorrasAlmenar, J. J.; Coronado, E.; Müller, A.; Pope, M. T. *Polyoxometalate Molecular Science*; Kluwer: Dordrecht, The Netherlands, 2004.

(24) Sadakane, M.; Dickman, M. H.; Pope, M. T. *Angew. Chem., Int. Ed.* **2000**, *39*, 2914.

(25) Mialane, P.; Lisnard, L.; Mallard, A.; Marrot, J.; AnticFidancev, E.; Aschehoug, P.; Vivien, D.; Sécheresse, F. *Inorg. Chem.* **2003**, *42*, 2102.

(26) Niu, J. Y.; Zhao, J. W.; Wang, J. P. *Inorg. Chem. Commun.* **2004**, *7*, 876.

(27) Wang, J. P.; Duan, X. Y.; Du, X. D. J.; Niu, Y. *Cryst. Growth Des.* **2006**, *6*, 2266.

(28) Bassil, B. S.; Dickman, M. H.; von der Kammer, B.; Kortz, U. *Inorg. Chem.* **2007**, *46*, 2452.

(29) Bassil, B. S.; Dickman, M. H.; Römer, I.; von der Kammer, B.; Kortz, U. *Angew. Chem., Int. Ed.* **2007**, *46*, 6192.

(30) Hussain, F.; Gable, R.; Speldrich, M.; Kögerler, P.; Boskovic, C. *Chem. Commun.* **2009**, 328.

(31) Niu, J. Y.; Wang, K. H.; Chen, H. N.; Zhao, J. W.; Ma, P. T.; Wang, J. P.; Li, M. X.; Bai, Y.; Dang, D. B. *Cryst. Growth Des.* **2009**, *9*, 4362.

(32) Reinoso, S.; GiménezMarqués, M.; Galán-Mascarós, J.; Vitoria, P.; GutiérrezZorrilla, J. M. *Angew. Chem., Int. Ed.* **2010**, *49*, 8384.

(33) Ritchie, C.; Boskovic, C. *Cryst. Growth Des.* **2010**, *10*, 488.

(34) Hussain, F.; Patzke, G. R. *CrystEngComm* **2011**, *13*, 530.

(35) Cui, K. Y.; Li, F. Y.; Xu, L.; Xu, B. B.; Jiang, N.; Wang, Y. C.; Zhang, J. P. *Dalton Trans.* **2012**, *41*, 4871.

(36) Ibrahim, M.; Mal, S. S.; Bassil, B. S.; Banerjee, A.; Kortz, U. *Inorg. Chem.* **2011**, *50*, 956.

(37) Ritchie, C.; Speldrich, M.; Gable, R. W.; Sorace, L.; Kögerler, P.; Boskovic, C. *Inorg. Chem.* **2011**, *50*, 7004.

(38) Zhang, S. W.; Wang, Y.; Zhao, J. W.; Ma, P. T.; Wang, J. P.; Niu, J. Y. *Dalton Trans.* **2012**, *41*, 3764.

(39) Wang, K.; Zhang, D. D.; Ma, J. C.; Ma, P. T.; Niu, J. Y.; Wang, J. P. *CrystEngComm* **2012**, *14*, 3205.

(40) Vonci, M.; Akhlaghi Bagherjeri, F.; Hall, P. D.; Gable, R. W.; Zavras, A.; O'Hair, R. A. J.; Liu, Y. P.; Zhang, J.; Field, M. R.; Taylor, M. B.; Du Plessis, J.; Bryant, G.; Riley, M.; Sorace, L.; Aparicio, P. A.; López, X.; Poblet, J. M.; Ritchie, C.; Boskovic, C. *Chem. - Eur. J.* **2014**, *20*, 14102.

(41) Wang, Y.; Sun, X. P.; Li, S. Z.; Ma, P. T.; Niu, J. Y.; Wang, J. P. *Cryst. Growth Des.* **2015**, *15*, 2057.

(42) Li, H. L.; Liu, Y. J.; Zheng, R.; Chen, L. J.; Zhao, J. W.; Yang, G. Y. *Inorg. Chem.* **2016**, *55*, 3881.

(43) Li, H. L.; Liu, Y. J.; Liu, J. L.; Chen, L. J.; Zhao, J. W.; Yang, G. Y. *Chem. - Eur. J.* **2017**, *23*, 2673.

(44) Sadakane, M.; Dickman, M. H.; Pope, M. T. *Inorg. Chem.* **2001**, *40*, 2715.

(45) Fang, X. K.; Anderson, T. M.; Benelli, C.; Hill, C. L. *Chem. - Eur. J.* **2005**, *11*, 712.

(46) Lu, Y.; Xu, Y.; Li, Y. G.; Wang, E. B.; Xu, X. X.; Ma, Y. *Inorg. Chem.* **2006**, *45*, 2055.

(47) Zimmermann, M.; Belai, N.; Butcher, R. J.; Pope, M. T.; Chubarova, E. V.; Dickman, M. H.; Kortz, U. *Inorg. Chem.* **2007**, *46*, 1737.

(48) Huang, L.; Cheng, L.; Fang, W. H.; Wang, S. S.; Yang, G. Y. *Eur. J. Inorg. Chem.* **2013**, *2013*, 1693.

(49) Ni, L. B.; Hussain, F.; Spingler, B.; Weyeneth, S.; Patzke, G. *Inorg. Chem.* **2011**, *50*, 4944.

(50) Zhang, S. W.; Zhang, D. D.; Ma, P. T.; Liang, Y. F.; Wang, J. P.; Niu, J. Y. *CrystEngComm* **2013**, *15*, 2992.

(51) Ma, P. T.; Wan, R.; Wang, Y. Y.; Hu, F.; Zhang, D. D.; Niu, J. Y.; Wang, J. P. *Inorg. Chem.* **2016**, *55*, 918.

(52) Kortz, U. *J. Cluster Sci.* **2003**, *14*, 205.

(53) Mialane, P.; Dolbecq, A.; Marrot, J.; Sècheresse, F. *Inorg. Chem. Commun.* **2005**, *8*, 740.

(54) Ju, W. W.; Zhang, H. T.; Xu, X.; Zhang, Y.; Xu, Y. *Inorg. Chem.* **2014**, *53*, 3269.

(55) Hu, F.; Ma, P. T.; Han, M. D.; Wan, R.; Wang, J. P.; Niu, J. Y. *Inorg. Chem. Commun.* **2016**, *67*, 103.

(56) Ritchie, C.; Baslon, V.; Moore, E. G.; Reber, C.; Boskovic, C. *Inorg. Chem.* **2012**, *51*, 1142.

(57) Ma, X.; Yang, W.; Chen, L. J.; Zhao, J. W. *CrystEngComm* **2015**, *17*, 8175.

(58) Zhang, Z. M.; Yao, S.; Qi, Y. F.; Li, Y. G.; Wang, Y. H.; Wang, E. B. *Dalton Trans.* **2008**, *37*, 3051.

(59) Zhang, Z. M.; Yao, S.; Li, Y. G.; Wang, Y. H.; Qi, Y. F.; Wang, E. B. *Chem. Commun.* **2008**, 1650.

(60) Yao, S.; Zhang, Z. M.; Li, Y. G.; Lu, Y.; Wang, E. B.; Su, Z. M. *Cryst. Growth Des.* **2010**, *10*, 135.

(61) Yao, S.; Zhang, Z. M.; Li, Y. G.; Wang, E. B. *Dalton Trans.* **2010**, *39*, 3884.

(62) Mal, S. S.; Dickman, M. H.; Kortz, U. *Chem. - Eur. J.* **2008**, *14*, 9851.

(63) Huang, L.; Cheng, L.; Fang, W. H.; Wang, S. S.; Yang, G. Y. *Eur. J. Inorg. Chem.* **2013**, *2013*, 1693.

(64) Godin, B.; Chen, Y. G.; Vaissermann, J.; Ruhlmann, L.; Verdaguer, M.; Gouzerh, P. *Angew. Chem., Int. Ed.* **2005**, *44*, 3072.

(65) Godin, B.; Vaissermann, J.; Herson, P.; Ruhlmann, L.; Verdaguer, M.; Gouzerh, P. *Chem. Commun.* **2005**, 5624.

(66) Yao, S.; Zhang, Z. M.; Li, Y. G.; Wang, E. B. *Dalton Trans.* **2009**, *38*, 1786.

(67) Zhao, H. Y.; Zhao, J. W.; Yang, B. F.; He, H.; Yang, G. Y. *CrystEngComm* **2014**, *16*, 2230.

(68) Zhang, Z. M.; Li, Y. G.; Wang, Y. H.; Qi, Y. F.; Wang, E. B. *Inorg. Chem.* **2008**, *47*, 7615.

(69) Zimmermann, M.; Belai, N.; Butcher, R. J.; Pope, M. T.; Chubarova, E. V.; Dickman, M. H.; Kortz, U. *Inorg. Chem.* **2007**, *46*, 1737.

(70) Contant, R.; Klemperer, W. G.; Yaghi, O. *Inorg. Synth.* **1990**, *27*, 104.

(71) Sheldrick, G. M. *SADABS: Program for Empirical Absorption Correction of Area Detector Data*; University of Göttingen: Göttingen, Germany, 1996.

(72) Sheldrick, G. M. *SHELXS 97, Program for Crystal Structure Solution*; University of Göttingen: Göttingen, Germany, 1997.

(73) Sheldrick, G. M. *SHELXL 97, Program for Crystal Structure Refinement*; University of Göttingen: Göttingen, Germany, 1997.

(74) Mal, S. S.; Kortz, U. *Angew. Chem., Int. Ed.* **2005**, *44*, 3777.

(75) Pichon, C.; Dolbecq, A.; Mialane, P.; Marrot, J.; Rivière, E.; Sécheresse, F. *Dalton Trans.* **2008**, *37*, 71.

(76) Boglio, C.; Lenoble, G.; Duhayon, C.; Hasenknopf, B.; Thouvenot, R.; Zhang, C.; Howell, R. C.; Burton-Pye, B. P.; Francesconi, L. C.; Lacôte, E.; Thorimbert, S.; Malacria, M.; Afonso, C.; Tabet, J. C. *Inorg. Chem.* **2006**, *45*, 1389.

(77) Contant, R.; Richet, M.; Lu, Y. W.; Keita, B.; Nadjo, L. *Eur. J. Inorg. Chem.* **2002**, *2002*, 2587.

(78) Brown, I. D.; Altermatt, D. *Acta Crystallogr., Sect. B: Struct. Sci.* **1985**, *41*, 244.

(79) Ritchie, C.; Baslon, V.; Moore, E. G.; Reber, C.; Boskovic, C. *Inorg. Chem.* **2012**, *51*, 1142.

(80) Zhou, J. M.; Shi, W.; Li, H. M.; Li, H.; Cheng, P. *J. Phys. Chem. C* **2014**, *118*, 416.

(81) Li, L. L.; Wang, Z. J.; Yang, Z. P.; Guo, Q. L. *Opt. Commun.* **2014**, *332*, 83.

(82) Zhou, J.; Xia, Z. G. *J. Mater. Chem. C* **2015**, *3*, 7552.

(83) Wang, Y. L.; Ma, Y.; Yang, X.; Tang, J.; Cheng, P.; Wang, Q. L.; Li, L. C.; Liao, D. Z. *Inorg. Chem.* **2013**, *52*, 7380.

(84) Petoud, S.; Muller, G.; Moore, E. G.; Xu, J.; Sokolnicki, J.; Riehl, J. P.; Le, U. N.; Cohen, S. M.; Raymond, K. N. *J. Am. Chem. Soc.* **2007**, *129*, 77.

(85) Ma, P. T.; Wan, R.; Si, Y. N.; Hu, F.; Wang, Y. Y.; Niu, J. Y.; Wang, J. P. *Dalton Trans.* **2015**, *44*, 11514.

(86) Fu, Z. L.; Xia, W. W.; Li, Q.; Cui, X. Y.; Li, W. H. *CrystEngComm* **2012**, *14*, 4618.

(87) Zhang, Y.; Gong, W. T.; Yu, J. J.; Pang, H. C.; Song, Q.; Ning, G. L. *RSC Adv.* **2015**, *5*, 62527.

(88) An, Z. B.; Xiao, X. Z.; Yu, J.; Mao, D. S.; Lu, G. Z. *RSC Adv.* **2015**, *5*, 52533.

(89) Watras, A.; Dereń, P. J.; Pązik, R. *New J. Chem.* **2014**, *38*, 5058.

(90) Xu, D. K.; Liu, C. F.; Yan, J. W.; Yang, S. H.; Zhang, Y. L. *J. Phys. Chem. C* **2015**, *119*, 6852.

(91) Zhang, Y. L.; Liu, X. H.; Lang, Y. B.; Yuan, Z.; Zhao, D.; Qin, G. S.; Qin, W. P. *J. Mater. Chem. C* **2015**, *3*, 2045.

(92) Song, L. M.; Wang, Q.; Tang, D. H.; Liu, X. H.; Zhen, Z. *New J. Chem.* **2007**, *31*, 506.

(93) Cichos, J.; Marciniak, L.; Hreniak, D.; Strek, W.; Karbowiak, M. *J. Mater. Chem. C* **2014**, *2*, 8244.

(94) Ito, T.; Yashiro, H.; Yamase, T. *Langmuir* **2006**, *22*, 2806.

(95) Shen, H. Y.; Wang, W. M.; Bi, Y. X.; Gao, H. L.; Liu, S.; Cui, J. Z. *Dalton Trans.* **2015**, *44*, 18893.

(96) Guillou, O.; Bergerat, P.; Kahn, O.; Bakalbassis, E.; Boubekeur, K.; Batail, P.; Guillot, M. *Inorg. Chem.* **1992**, *31*, 110.

(97) Tan, X. F.; Zhou, J.; Fu, L. S.; Xiao, H. P.; Zou, H. H.; Tang, Q. L. *Dalton Trans.* **2016**, *45*, 5253.

(98) Guo, Y. N.; Xu, G. F.; Gamez, P.; Zhao, L.; Lin, S. Y.; Deng, R.; Tang, J.; Zhang, H. J. *J. Am. Chem. Soc.* **2010**, *132*, 8538.

(99) Bag, P.; Rastogi, C. K.; Biswas, S.; Sivakumar, S.; Mereacre, V.; Chandrasekhar, V. *Dalton Trans.* **2015**, *44*, 4328.

(100) Li, Y. Y.; Gao, F.; Beves, J. E.; Li, Y. Z.; Zuo, J. L. *Chem. Commun.* **2013**, *49*, 3658.

(101) Woodruff, D. N.; Winpenny, R. E.; Layfield, R. A. *Chem. Rev.* **2013**, *113*, 5110.

(102) Feng, X. J.; Han, H. Y.; Wang, Y. H.; Li, L. L.; Li, Y. G.; Wang, E. B. *CrystEngComm* **2013**, *15*, 7267.

(103) Lin, S. Y.; Zhao, L.; Guo, Y. N.; Zhang, P.; Guo, Y.; Tang, J. *Inorg. Chem.* **2012**, *51*, 10522.

(104) Ma, P. T.; Hu, F.; Wan, R.; Huo, Y.; Zhang, D. D.; Niu, J. Y.; Wang, J. P. *J. Mater. Chem. C* **2016**, *4*, 5424.

(105) Chen, Q.; Meng, Y. S.; Zhang, Y. Q.; Jiang, S. D.; Sun, H. L.; Gao, S. *Chem. Commun.* **2014**, *50*, 10434.

(106) Guo, Y. N.; Xu, G. F.; Wernsdorfer, W.; Ungur, L.; Guo, Y.; Tang, J.; Zhang, H. J.; Chibotaru, L. F.; Powell, A. K. *J. Am. Chem. Soc.* **2011**, *133*, 11948.

(107) Ibrahim, M.; Mereacre, V.; Leblanc, N.; Wernsdorfer, W.; Anson, C. E.; Powell, A. K. *Angew. Chem., Int. Ed.* **2015**, *54*, 15574.